UNIVERSITY OF SALENTO

DEPARTMENT OF PHYSICS

Ph.D. Thesis:

STUDIES OF PHOTOEMISSION FROM METAL CATHODES WITH MICRO-ROUGH SURFACE: SCHOTTKY EFFECT AND PLASMA PRODUCTION INFLUENCE

Tutor: Prof. V. Nassisi

Ph.D. Student:
Giuseppe Caretto

XX Course (2005 - 2007)

Table of contents

PREFACE

The present work, performed since 2005 to 2007, has been dedicated to the development of a "good" system of electron photoemission that uses metal targets irradiated by excimer lasers. This research project has been mainly realized in the Applied Electronics Laboratory, at the Department of Physics of the University of Salento. The attention has been focused on the techniques to enhance the electron emission efficiency, in order to obtain electron beams of high intensity. Low angular divergence and short time duration of the extracted beams are other objectives of this work. In particular, this study wishes to lead to the optimization, for the realization of new and versatile accelerators, useful for application in the fields of:

- new scientific devices such as free-electron lasers (FEL)
- X-ray machines
- electron beam therapy machines
- high power microwave generators
- controlled thermonuclear fusion reactors
- collective ion accelerators for basic physics studies and medical therapies.

Therefore, the photo-extraction process under different experiment conditions has been carefully investigated. Namely we studied the electron emission of a sample as a

function of experimental controlled parameters, like the target material, its superficial morphology, the accelerating voltage, the wavelength and the fluence of the used laser.

During the thesis work, this phenomenon was studied by means of three excimer UV lasers of short wavelengths: KrF at 248 nm, XeCl at 308 nm and KrCl at 222 nm wavelength; regarding to the materials used like cathodes in the experiments, they were mostly yttrium and zinc.

To comprehend the processes concerning the photoemission it is necessary to develop a fine electron-beam extraction system. It is important to find if, changing the experimental conditions, there is a real possibility to increase the number of the extracted electrons from metal target. In particular, the surface morphology variations of the cathode and its influence on the charge yield were analyzed.

Samples with natural and induced surface roughness were examined. Micro superficial irregularities were simply created and their effect on photoemission process studied in detail.

Using a fast oscilloscope the pulsed current signals and the incident laser waveforms were recorded; measurements and analyses have been carried out on photo-emitted current, temporal quantum efficiency, electron spatial distribution, and temporal behavior under laser action.

Moreover, a theoretical model has been formulated, which allows one to estimate the results for a real surface profile and to predict the current and the efficiency for particular morphologies that will be realized and used in the future.

To confirm the performed calculations, simulation code OPERA 3D was used. Using this one it is possible to plan the anode-cathode gap and to let the different

voltages on the surfaces; starting the estimation process, several experimental parameters were evaluated and confronted with the real ones.

Future work could be the realization of finer superficial roughness, one-two order lower, hoping to increase more and more the electron-beam intensities.

In the Chapter 1 there is the development of the equations that govern the electron photoemission process. In particular, thermionic emission, field-effect emission and photo-emission will be treated; the reduction of the work function of the metal (Schottky effect) plays a fundamental role in the photocurrent calculation.

In the Chapter 2 the whole experimental apparatus is described in details: the vacuum chamber, the targets, the diagnostic system, and the way to record the laser and current pulses. Complete description of the characteristics of excimer lasers are made: the active medium, the laser chamber, the pumping systems used, the duration and the shape of the laser pulses.

In the Chapter 3 the experimental results concerning the efficiency and the photocurrent for different metal targets, irradiated by different excimer lasers are reported.

In the Chapter 4 a theoretical model and an electronic simulation of an extraction-acceleration system is presented. Choosing appropriate parameters, it is possible to correlate the results obtained to the ones carried out from the experimental measurements, in order to confirm the given interpretation of phenomena that govern the photoemission process.

In the Chapter 5 there is a discussion of all the results and a comparison between different types of cathodes (changing work function, thickness, and superficial morphology) and different laser wavelength.

Furthermore, during the Ph. D. course several publications on paper and proceedings for conferences participations have been made:

I. F. Belloni, G. Caretto, A. Lorusso, V. Nassisi, M.V. Siciliano, "Photo-emission studies from Zn cathodes under plasma phase", ***Radiation Effects and Defects in Solids***, **160**, p 587-594, 2005.

II. G. Caretto, D. Doria, V. Nassisi and M.V. Siciliano, "Photoemission studies from metal by UV lasers", ***Journal of Applied Physics***, **101**, 73109-73116, 2007.

III. G. Caretto, L. Martina, V. Nassisi, M.V. Siciliano, "Behavior of photocathodes on superficial modification by electrical breakdown", ***Nuclear Instruments and Methods B***, 2007 (in press).

IV. G. Caretto, L. Martina, V. Nassisi and M.V. Siciliano**,** "Temporal behavior of photoemission for Yttrium cathodes" ***Radiation Effects and Defects in Solids***, **163**, 2008.

V. G. Caretto, P. Miglietta, V. Nassisi, A. Perrone and M.V. Siciliano**,** "Photoelectron performance of Y thin films and Y smooth bulk", ***Radiation Effects and Defects in Solids***, **163**, 2008.

VI. F. Belloni, G. Caretto, A. Lorusso, V. Nassisi, A. Perrone and M.V. Siciliano, "Photo-emission studies from Zn cathodes under plasma phase", *PPLA II, Giardini Naxos, Catania, Italy*, June 8-11, 2005.

VII. F. Belloni, G. Caretto, D. Doria A. Lorusso, V. Nassisi, A. Perrone, M.V. Siciliano, "Studio dell'evoluzione temporale dell'efficienza quantica di un fotocatodo metallico", *XCI Congresso Nazionale SIF, Catania, Italy*, September 26 - October 1, 2005.

VIII. V.Nassisi, G.Caretto, A.Lorusso, D.Doria, F. Belloni and M.V.Siciliano, "Temporal quantum efficiency of a micro-structured cathode", *EPAC 06, Edimburgh, Scotland*, June 26-30, 2006.

IX. D. Doria, F. Belloni, A. Lorusso, G. Caretto, V. Nassisi and M.V. Siciliano, "Plasma influence on photoemission from metal by UV lasers", *ESCAMPIG XVIII, Lecce, Italy*, July 12-15, 2006.

X. F. Belloni, G. Caretto, D. Doria, A. Lorusso, V. Nassisi, P. Espositivo, V. Nicolardi, "Compressori di corrente e tensione e nuovi circuiti di amplificazione con linee di trasmissione", *XCII Congresso Nazionale SIF, Torino, Italy*, September 18-23, 2006.

XI. G. Caretto, L. Martina, V. Nassisi and M.V. Siciliano**,** "Temporal behavior of photoemission for Yttrium cathodes", *PPLA III, Scilla, Reggio Calabria, Italy*, June 14-16, 2007.

XII. G. Caretto, P. Miglietta, V. Nassisi, A. Perrone and M.V. Siciliano**,** "Photoelectron performance of Y thin films and Y smooth bulk, *PPLA III, Scilla, Reggio Calabria, Italy*, June 14-16, 2007.

XIII. G. Caretto, V. Nassisi, M.V. Siciliano, "Role of plasma in temporal behaviour for Y cathodes", *ICPIG XXVIII, Praga, Czech Republic*, July 15-20, 2007.

XIV. G. Caretto, V. Nassisi and M.V. Siciliano, "Electron emission performance of yttrium cathodes by UV lasers", *HEP 07, Manchester, England*, July 19-25, 2007.

XV. G. Caretto, L. Martina, V. Nassisi and M.V. Siciliano**, "**Behavior of photocathodes on superficial modification by electrical breakdown", *ECAART IX, Firenze, Italy*, September 2-5, 2007.

XVI. G. Caretto, P. Miglietta, V. Nassisi, A. Perrone, M.V. Siciliano, "Studio di fotoemissione da catodi di ittrio", *XCIII Congresso Nazionale SIF, Pisa, Italy*, September 24-29, 2007.

1 Electron emission from metals

1.1 Introduction

In this chapter the fundamental physical laws that govern the electron emission from solids and, in particular, from metals are presented. In details, thermionic effect, field effect and photoelectric effect will be discussed and analyzed; Schottky effect will be considered, being it responsible of tangible variations of the extracted electrons number.

1.2 Metals properties

According to the *"free electron model"* [1], it is possible to consider the external electronic shells of metal atoms like free fermions gas. In fact, these ones can move in the whole solid and feel less the interaction with the nuclei, because of the shield effect due to the internal shells. Macroscopically, one can suppose that the metal forms an almost equipotential structure for the conduction electrons, that suffer only little

perturbations of their free path, because of interactions with the lattice ions and the others electrons. In this model the electron energy is due simply to its kinetic energy and it is feasible to think the metal like a potential hole deep E_s: the electron is able to leave the metal surface if its kinetic energy is greater than E_s (figure 1.1).

The free electron energy distribution $\rho(E,T)$ is defined like the electron number for energy unit and for volume unit at T temperature. The knowledge of this quantity is important because allows to establish if inside of the metal there are fermions able to overcome the potential barrier.

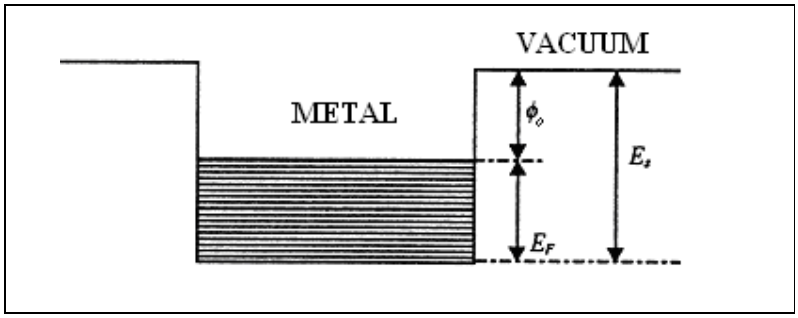

Figure 1.1 - Schematic representation of the potential hole in the free-electron model. E_s is the minimum energy necessary for electron to get out from the metallic surface, ϕ_0 is known like the metal work function**.**

By quantum calculation, being the electron a half integer spin particle (fermion), one can write the energy distribution as

$$\rho(E,T) = N(E) f(E,T) \qquad (1.1),$$

where $N(E)$ is the state density and $f(E,T)$ is the Fermi-Dirac distribution, namely the probability that a fermion has got energy E at the temperature T ; all the energy values have to be referred to the bottom of the potential hole.

The expression for the Fermi-Dirac distribution is

$$f(E,T) = \frac{1}{1+e^{\frac{E-E_F}{kT}}} \qquad (1.2),$$

where k is the Boltzmann constant, T is the solid temperature and E_F is the Fermi level, that corresponds to the energetic state that has probability ½. In opposition to the classical theory, at temperature $T = 0\ K$ some electrons may have no-zero energy; this fact is due to the Pauli Exclusion Principle. For $T > 0\ K$ the levels with energies higher than E_F begin to populate; the level E_F can be interpreted like the fermionic maximum energy reached at the absolute zero temperature.

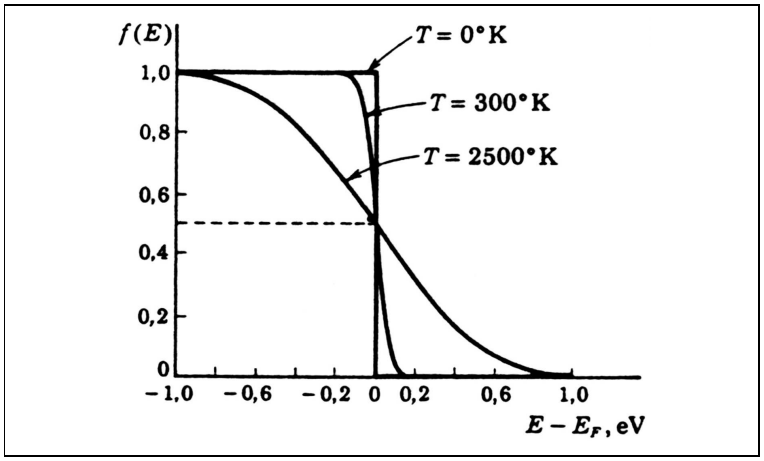

Figure 1.2 - Fermi–Dirac distribution function for different temperature values.

The state density is the number of the electrons per volume unit at fixed energy; it can be written as

$$N(E) = \frac{8\pi}{h^3}(2m)^{\frac{3}{2}}E^{\frac{1}{2}} \qquad (1.3),$$

where *m* is the electron mass and *h* is the Planck constant. Utilizing the expressions (1.2) and (1.3) it has been obtained the final formula for the energy distribution of free electrons

$$\rho(E,T) = \frac{8\pi}{h^3}(2m)^{\frac{3}{2}}\left(\frac{E^{\frac{1}{2}}}{1+e^{\frac{E-E_F}{kT}}}\right) \qquad (1.4),$$

as plotted in figure 1.3.

The function $\rho(E,T)$ shows a small dependence with the temperature; the only effect due to the temperature is the changing of the electron concentration in the neighborhood of Fermi energy from lower to higher energetic levels. E_F can be considered like a constant depending on little temperature changing.

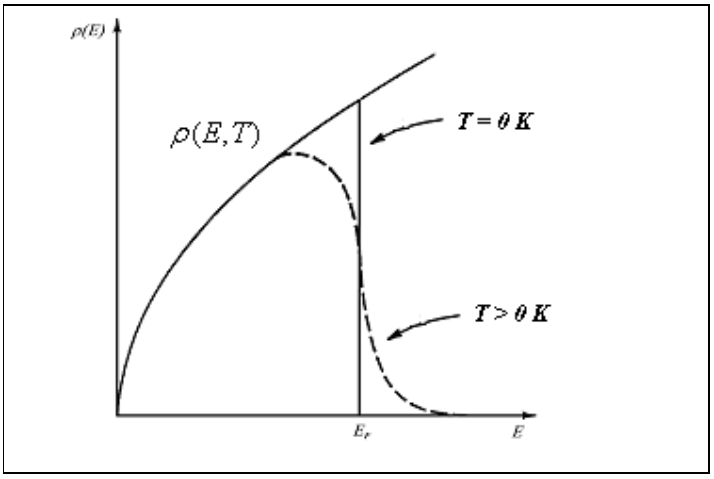

Figure 1.3 - State density as a function of the energy for a free electron gas.

One of the most important property for the solids and in particular for the metals is their work function $\phi_0 = E_s - E_F$ (figure 1.4), defined like the minimum energy

necessary for an electron to overcome the potential barrier at 0 K temperature. It is of the order of few eV and depends on the material that composes the solid.

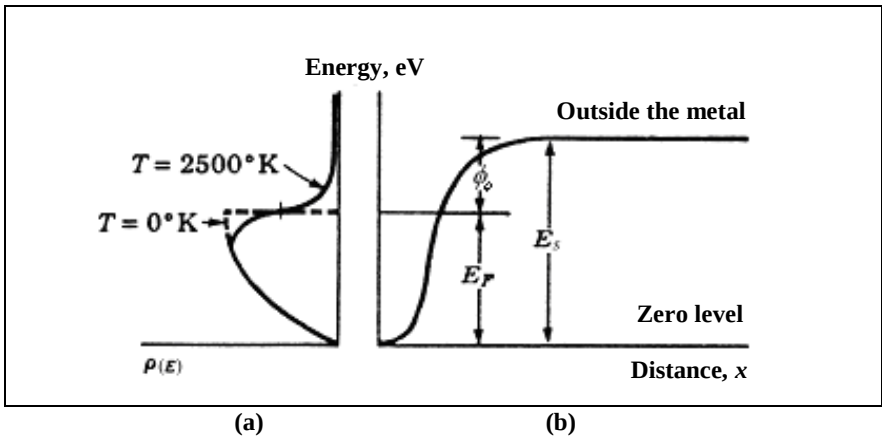

Figure 1.4 - (a) State density for two different values of temperature.
(b) Potential wall onto the metal surface.

The work function is not fixed; it depends on the roughness and on the presence of imperfections in the crystal lattice. It plays a fundamental role in the phenomena correlated to the emission of electrons from the surface of a solid: photoemission, thermionic effect, field emission or electron transfer from a metal to the other (contact potential).

1.3 Thermionic emission

This process allows to get electrons by increasing the target temperature. In this way the $\rho(E,T)$ function assumes high values for $E > E_F$ and electrons can leave the metal surface.

Also for temperatures near to the melting point of metal (~ $10^3\,K$) few electrons are extracted, therefore at room temperature (≅ 300 K), the probability that an electron is able to rise above the potential barrier is very low.

The expression for the current density by thermionic emission is

$$J_o = \frac{4\pi m e k^2 T^2}{h^3} e^{-\frac{\phi_0}{kT}} \qquad (1.5).$$

If one lets

$$A = \frac{4\pi m e k^2}{h^3} \approx 120 \quad \left[\frac{A}{cm^2 K^2}\right],$$

the equation (1.5) can be simply written as

$$J_o = AT^2 e^{-\frac{\phi_0}{kT}} \qquad (1.6),$$

well known like Dushman–Richardson equation [2].

The space-charge effect in the area of emitted electrons is the primary responsible of a significant reduction of the current density for all the extraction processes.

The (1.6) formula is effective in the saturation regime, namely the state with high electric fields applied, in order to annihilate the space-charge effect.

1.4 Schottky effect

If an external electron is near a metallic surface connected to the ground, the metal polarizes itself and induces attractive forces on the electron. Until the distance *z* electron-surface is greater than the interatomic dimension, *image charge method* can be used in order to calculate its potential energy [3]

$$V_{img} = -\frac{e^2}{4z} \qquad (1.7),$$

represented by *AB* curve plotted in figure 1.5.

The model proposed by Schottky supposes that this potential energy is valid for distances $z > z_o$, assuming a constant force for $0 < z < z_o$, where z_0 is a critical distance, function of the material; in this region the potential energy of the electron is a linear function of *z* (*CA* line in figure 1.5).

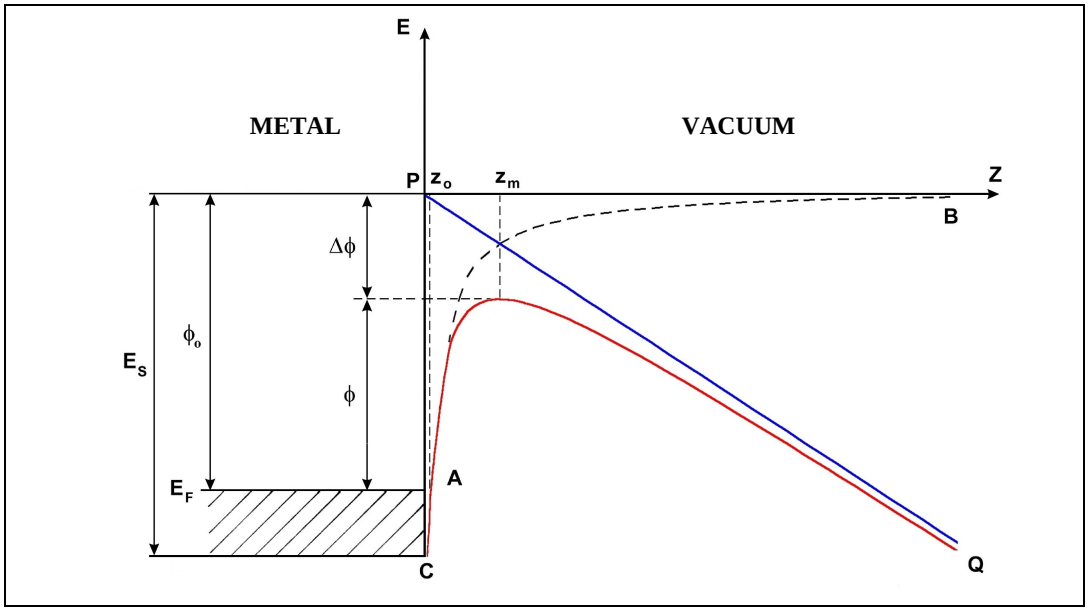

Figure 1.5- Surface potential wall for field-effect.

If the metal is undergone to an intense external electric field, the work function decreases; this phenomenon is known like *Schottky effect*. Supposing a homogeneous field *F*, the total potential energy of the electron is the sum of the image potential and the one due to the applied field

$$V(z) = -\frac{e^2}{4z} - eF\,z \tag{1.8}.$$

This function (red curve in figure 1.5) has its maximum at $z = z_m$, where

$$z_m = \frac{1}{2}\sqrt{\frac{e}{F}} \tag{1.9}.$$

From *V(z)* expression it is possible to obtain the equation for work function reduction in presence of external electric field

$$\Delta\phi_0 = V(z_m) = -\,e\sqrt{eF} \tag{1.10}.$$

Therefore, the Richardson-Dushman equation (1.6) can be rewritten in its generalized form, which contains a correction factor due to the applied electric field

$$J_s = AT^2 \exp\left(-\frac{\phi_0 - e\sqrt{eF}}{kT}\right) \tag{1.11}.$$

This one has a good compatibility with experimental data if it is considered a mirror-like surface, instead for oxidized and rough surface [4] it is necessary to introduce a new correction

$$J_s = AT^2 \exp\left(-\frac{\phi_0 - e\, f\sqrt{eF}}{k\,T}\right) \tag{1.12}$$

where *f* is an empiric coefficient (*f >1*) that rules the emission increasing for a real surface. In fact, the cathode surface it is not perfectly smooth, being produced by sand-blasting or polisher machines. The Schottky effect influences all the others emission processes.

1.5 Field-emission effect

In presence of very intense electric field, namely of the order of 10^6 *V/cm* or more, the *field emission* effect occurs, very different than the Schottky one. In this case electrons, because of tunneling process, cross the potential barrier at the metal surface [5]. From quantum considerations, the emitted current density J_c can be evaluated by integrating the product function between the flow $n(E_z)$ of incident electron on the surface and the probability $P(E_z)$ of penetration of electron into the potential barrier $V(z)$, on the whole range of electron energy.

$$J_c = \int_{-\infty}^{+\infty} e\, n(E_z)\, P(E_z)\, dE_z \tag{1.13},$$

where $E_z = \frac{p_z^2}{2m} + V(z)$ is the electron energy related to its motion along the *z* direction, *e* is the electron charge and p_z is the z component of the moment.

The expression for $n(E_z)$ can be obtained from Fermi – Dirac statistic, if one considers the free electron model for conduction electrons

$$n(E_z) = \frac{4\pi m k T}{h^3} \ln\left(1 + e^{-\frac{E_z - E_F}{kT}}\right) \tag{1.14}.$$

The probability of penetration through the potential barrier is determined by solving the time-independent Schrödinger equation, for an electron moving in *z* direction

$$\frac{d^2\psi}{dz^2} + \frac{2m}{\hbar^2}\left[E_z - V(z)\right]\psi = 0 \tag{1.15}.$$

For one-dimension potential the model proposed by Schottky [3] can be used:

$$V(z) = \begin{cases} -V_o & se \quad z < 0 \\ -\dfrac{e^2}{4z} - eF\,z & se \quad z > 0 \end{cases} \tag{1.16},$$

where V_o is a constant lower than Fermi energy E_F. Solving the equation (1.15) it is possible to have an approximate expression for the probability $P(E_z)$

$$P(E_z) = \exp\left[-\frac{4\,g(y)}{3\hbar e F}\left(2m\left|E_z\right|^3\right)^{\frac{1}{2}}\right] \tag{1.17},$$

where *g* is a tabulated function of $y = \dfrac{\left(e^3 F\right)^{\frac{1}{2}}}{\left|E_z\right|}$ [5].

For low temperatures ($T \to 0$), namely for electron energies nearest to Fermi level, by insert (1.14) and (1.17) into the (1.13), it is possible to obtain current density carried out for field emission

$$J_c = \frac{e^3}{8\pi h|E_F|t^2(y_F)} F^2 \exp\left[-\frac{4g(y_F)}{3\hbar e F}\left(2m|E_F|^3\right)^{\frac{1}{2}}\right] \qquad (1.18),$$

where *t* is a tabulated function of $y_F = \frac{\left(e^3 F\right)^{\frac{1}{2}}}{|E_F|}$ [6].

For relatively low electric field ($F < 10^7$ *V/cm*) the functions $g(y_F)$ and $t(y_F)$ can be approximated to 1, simplifying once more the (1.18):

$$J_c = BF^2 e^{-\frac{\beta}{F}} \qquad (1.19),$$

where $B = \frac{e^3}{8\pi h|E_F|}$ and $\beta = \frac{4}{3\hbar e}\left(2m|E_F|^3\right)^{\frac{1}{2}}$.

If one works at sufficiently low temperatures, the field emission presents only a little difference with the limit case $T = 0$. When the temperature reaches values of 10^3 *K*, the equation (1.19) is not valid, because of the contribution due to the electrons that overcome the Fermi level.

1.5.1 Resistive heating by field effect

The surface of an electrode is never perfectly mirror-like. In real cases the presence of tips and whiskers (figure 1.6a) in the surface geometry enhances the electric field strength, even at relatively low voltages.

Almost all metallic surfaces present microscopic whiskers with height of the order of 10^{-4} *cm* and base of the order of 10^{-5} *cm*. Their density is usually in the range 1 - 10^{4} whiskers/cm^2.

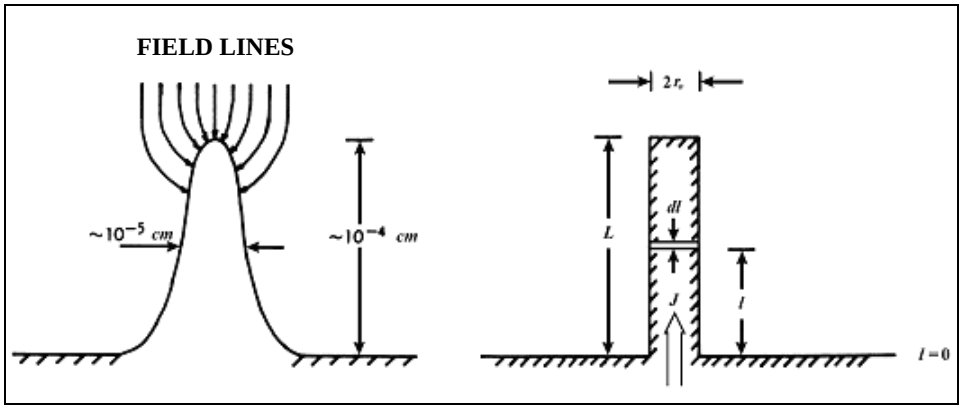

(a) **(b)**

Figure 1.6: (a) Electric field lines on the tip of the whisker. (b) Heat flow for a cylindrical emitter**.**

If high voltage is applied to the metal, the electric field strength on the tip of the whiskers can be even two orders of magnitude greater than the equivalent macroscopic electric field, inducing noteworthy electron emission by field-effect and local superficial heating.

For theoretical study of heat flow in the case of field emission, one can considers a simple cylindrical emitting (figure 1.6b). The temperature variation in the infinitesimal volume element $dV = \pi r_o^2 dl$ is

$$\frac{\partial T}{\partial t} = \frac{1}{\rho c \pi r_o^2 dl} \frac{dQ}{dt} \qquad (1.20),$$

where ρ is the mass density, c the specific heat of the material, r_o is the cylinder radius and $\frac{dQ}{dt}$ the heat flow in the volume element. Considering the resistive generation of heat (Joule effect) and the thermic conduction, the heat flow [7] is

$$\frac{dQ}{dt} = \left.\frac{dQ}{dt}\right|_{Joule} + \left.\frac{dQ}{dt}\right|_{cond} \qquad (1.21),$$

where

$$\left.\frac{dQ}{dt}\right|_{Joule} = J^2 \eta \pi r_o^2 dl \qquad (1.22a),$$

$$\left.\frac{dQ}{dt}\right|_{cond} = K \pi r_o^2 \left(\left.\frac{\partial T}{\partial l}\right|_{+} - \left.\frac{\partial T}{\partial l}\right|_{-} \right) \qquad (1.22b),$$

J is the current density, l the distance from the base of the whisker, while η and K are the electric resistivity and the thermic conductibility of the material respectively. The terms $\left.\frac{\partial T}{\partial l}\right|_{+}$ and $\left.\frac{\partial T}{\partial l}\right|_{-}$ are, respectively, the temperature gradient in the l positive and l negative direction.

By placing the expressions (1.22) into the (1.20), it is possible to obtain the following equation

$$\frac{\partial^2 T}{\partial l^2} - \frac{\rho c}{K}\frac{\partial T}{\partial t} = -\frac{J^2 \eta}{K} \qquad (1.23),$$

whose solution is

$$T = -\frac{J^2 \eta}{2K} l^2 + c_1 l + c_2 \qquad (1.24).$$

For a particular choose of the boundary conditions,

$$\begin{cases} T = 0 & if \quad l = 0 \\ \dfrac{\partial T}{\partial l} = 0 & if \quad l = L \end{cases}$$

the maximum temperature at the top of the emitter ($l = L$) is

$$T_{\max} = \frac{J^2 \eta}{2K} L^2 \qquad (1.25).$$

The current density required to get $T_{\max}$ near the melting point of the material is of the order of $10^7 \div 10^8$ *A/cm*^{2}. It is essential to highlight that because of the tips distributions, the effective emitting area is smaller than the whole metal surface; therefore the total current density is different to *J* and is of the order of $1 \div 10$ *A/cm*^{2}.

The strong heating of the emitter can induce material vaporization with local production of plasma characterized by quick hydrodynamic extension [8, 9] (few *cm/*μ*s*).

1.6 Photoemission from metals

When an electron in the conduction band absorbs an electromagnetic energy $h\nu$, it is well known that its kinetic energy may be enough to overcome the potential barrier. This phenomenon is well known like *photoelectric emission*. If the temperature of the system is T = 0 K, theoretically the electron extraction can occur only if $h\nu > \phi_0$. In this case, in fact, the electrons have the Fermi energy and, after the photon absorption, they will have got energy $E > E_s$ - E_F, needed to the photoemission. By placing $\nu_0 = \frac{\phi_0}{h}$ and being $E_s = E_F + \phi_0$, it is evident than only electromagnetic waves with frequency $\nu \geq \nu_0$ are able to excite electrons over the level E_s. The photoelectric effect is, therefore, a threshold process.

For temperatures $T > 0K$ it is possible to have emission even if $\nu < \nu_0$, namely utilizing photons by energies lower than the metal work function. In fact, as seen above, over the absolute zero of temperature a little amount of electrons populates energetic states higher than the Fermi level. So, by interactions with photons of energies not much smaller than the work function, they may be able to prevail over the potential barrier.

The photoelectric effect is based on a physical process not applying in the case of free electron model. In fact, if one considers the process of collision involving a free electron, initially blocked relatively to the laboratory reference system, and one photon of energy E_o and momentum p_o. The inelastic scattering photon-electron is supposed occurring along the x direction of reference orthogonal to the metal surface. By

applying the energy and impulse conservation formulas, in the case of complete absorption of photon by electron

$$\begin{cases} E_o = E_e \\ p_o = p_e \end{cases} \qquad (1.26),$$

where E_e and p_e are, respectively, energy and momentum of electron after collision. The electron total energy after scattering will be

$$E_{Tot} = E_e + mc^2 \qquad (1.27),$$

where mc^2 is the electron rest energy. The total energy can be written like a function of the momentum p_e

$$E_{Tot}^2 = c^2 p_e^2 + \left(mc^2\right)^2 \qquad (1.28).$$

By matching the expressions (1.27) and (1.28), by utilizing the (1.26), it is possible to obtain $p_o^2 + 2c\, p_o m_e = p_e^2$, namely

$$p_e = \sqrt{p_o^2 + 2c\, p_o m_e} > p_o \qquad (1.29).$$

This one is not coherent with the momentum conservation law (1.26).

The electron-photon scattering phenomena in a metal are more complex than a simply collision between two particles. It is, in fact, necessary to take in account the contribution due to the crystal lattice in addition to the concept of the potential barrier.

So that an electron may be liberated in the vacuum after the photon interaction, the momentum component p_x orthogonal to the metal surface has to be

$$\frac{p_x^2}{2m} + h\nu > E_s \tag{1.30}$$

One can obtain that the photoelectric current density, per radiation intensity unit, is proportional to the so-called Fowler function [10]

$$F = \frac{4\pi m e kT}{h^3} \int_{E_s - h\nu}^{+\infty} \ln\left[1 + e^{\frac{(E_F - E)}{kT}}\right] dE \tag{1.31},$$

where $E = \frac{p_x^2}{2m}$.

By placing $\gamma = \frac{E - E_s + h\nu}{kT}$ and $\delta(t) = \frac{nh\nu - \phi_0}{kT(t)}$, the expression (1.31) becomes

$$F(\delta) = \frac{4\pi m e (kT)^2}{h^3} \int_0^{+\infty} \ln\left[1 + e^{\delta - \gamma}\right] dx \tag{1.32}.$$

The analytical expression of the integral in the (1.32) is given by the following series [11]

$$F(\delta) = \begin{cases} \sum_{n=1}^{+\infty} \frac{e^{n\delta}}{n^2} (-1)^{(n-1)} & se \quad \delta \le 0 \\ \frac{\pi^2}{6} + \frac{\delta^2}{2} - \sum_{n=1}^{+\infty} \frac{e^{-n\delta}}{n^2} (-1)^{(n-1)} & se \quad \delta \ge 0 \end{cases} \tag{1.33}.$$

An important parameter that influences the cathode chosen for electron extraction is the *quantum efficiency*, defined by

$$\eta = \frac{Number\ of\ \ photoemitted\ electrons}{Number\ of\ incident\ photons} \qquad (1.34).$$

The materials with the highest values of quantum efficiency, under the same experimental conditions, are the metals and the semiconductors. In metallic photocathodes η varies from 10^{-5} to 10^{-7}, in semiconductors it reached values of 10^{-2}. The remarkable difference is mainly due to higher reflectivity value of the metal surface than the semiconductor one, at the UV wavelengths.

Furthermore, before to reach the surface, the more internal metal electrons dissipate probably the excess energy absorbed from photons, because of enormous number of collisions with others electrons and crystal lattice impurities. In the case of metals, only the electrons nearest to the surface can be involved to the extraction process.

In the semiconductors [12], instead, the electrons lose energy by means of the interactions with lattice phonons. The lost energy is, in this case, a little amount of the one absorbed: by a consequence even the most internal electrons are able to release themselves through the semiconductor surface.

The semiconductor cathodes like GaN/InGaN or AlGaN/InGaN (hetero-epitaxial) present high quantum efficiency: 40% at 250 nm wavelength [13]. They, besides, work only at very high vacuum level, since a little contamination could damage and make them not working for these applications.

Although the quantum efficiency is higher in semiconductors, they are difficult to construct. The metallic photocathodes present many advantages of other nature: low

vacuum conditions, little cost of realization, better ease of handling, short response time and the possibility to be used for long time without modify their characteristics.

Furthermore, the principal advantage is that the electron beam parameters (intensity, time duration, angular spread) can be controlled easily by modifying the target work function and the laser source characteristics (wavelength, time duration, pulse shape, spot area).

1.6.1 Multi-photon process

More detailed studies of photoemission phenomenon [14] provide a general relation that includes possible non-linear effect (multi-photon process). The more generalized Fowler-DuBridge equation, modified by Bloembergen and Betchel [15], represents an evaluation of the total photo-current density

$$J(t) = \sum_{n=0}^{N+1} J_n(t) \qquad (1.35),$$

with

$$J_n(t) = \alpha_n A I^n(t)(1-R)^n T^2(t) F[\delta(t)] \qquad (1.36).$$

In the equation the current density $J_o = AT^2 e^{-\frac{\phi_0}{kT}}$ is due to the thermionic emission, A is the Richardson constant whose value is 120 A/(K^{2}cm^2) and ϕ_0 is the metal work function, while J_1, J_2,…, J_n are the current densities due to the one and more-

photons processes. The coefficients α_n are related to quantum phenomena concerning the multi-photon emission (α_o = 1 in the ideal case), $I(t)$ is the incident radiation intensity, R is the metal reflectivity, $T(t)$ is the target temperature and $F[\delta(t)]$ is the Fowler function with argument $\delta(t) = \frac{nh\nu - \phi_0}{kT(t)}$, k is the Boltzmann constant, while N represents the nearest integer smaller than $\frac{\phi_0}{h\nu}$.

The multi-photon effect consists mostly in the simultaneous absorption of two or more photons. This process allows us to observe photoelectrons even if it is $h\nu < \phi_0$ and the temperature T is so low that allows only electrons in the neighbourhood of the Fermi level E_F to populate states of higher energy. In qualitative way, it is possible to consider that, for a two-photon process (ϕ_0 not very lower than $h\nu$) (figure 1.7), it is $h\nu < \phi_0 < 2h\nu$, while in the case of the absorption of n photons [16] has to be $h\nu < \phi_0 < nh\nu$.

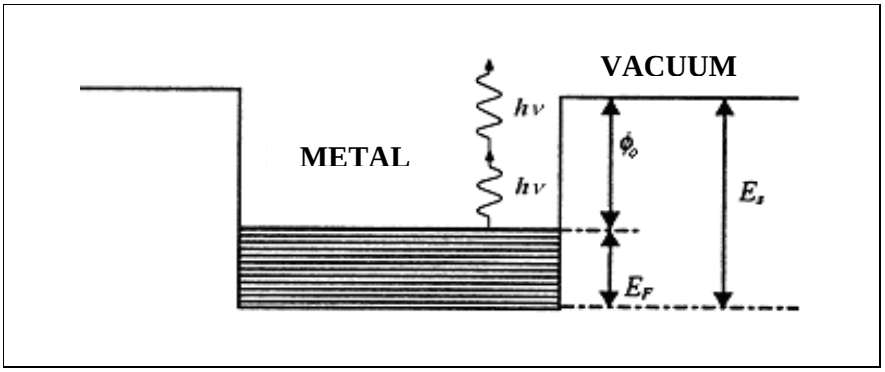

Figure 1.7: Schematic representation of two-photon photoemission process. The simultaneous absorption of two photons allows to the electron to overcome the potential barrier ($2h\nu > \phi_0$).

For $h\nu < \phi_0$, the electron emission is due to multi-photon processes and the total current is the sum of the thermionic component

$$J_0 = AT^2 \exp(-\phi_0 / kT) \qquad (1.37),$$

the components for the n-photon process, in the case $n <$ N+1

$$J_n(t) \cong a_n I^n(t)(1-R)^n J_0 \exp(nh\nu / kT) \qquad (1.38)$$

and the component due to the highest multi-photon process, for n = N+1

$$J_{N+1} \cong a_{N+1} A I^{N+1}(t) T^2 (1-R)^{N+1} \times \left[\frac{1}{2} \left(\frac{(N+1)h\nu - \phi_0}{kT} \right)^2 + \frac{\pi^2}{6} \right] \qquad (1.39).$$

In the case $h\nu > \phi_0$, from the theory the emission has got only two terms, because of zero value of N. Therefore there is only the thermionic term

$$J_0 = AT^2 \exp(-\phi_0 / kT), \qquad (1.40)$$

and the term

$$J_1 \cong a_1 A I(t) T^2 (1-R) \times \left[\frac{1}{2} \left(\frac{h\nu - \phi_0}{kT} \right)^2 + \frac{\pi^2}{6} \right] \qquad (1.41).$$

For this work the thermionic component was neglected, because the maximum temperature reached by the cathodes is of the order of 10^2 *K*.

1.7 Emittance and Brightness

The emittance is a quality fundamental parameter for all electron beams. It is related, to the pattern that the beam particles occupy within the six-dimension phase space. In many practical cases (where the magnetic vector potential is zero) the three coordinate pairs within the entire phase space are completely decoupled. Choosing z along the beam direction and supposing, for simplicity, a cylindrical symmetry problem, all the conclusions for transverse x-direction are the same than the ones for the y-direction. Assuming that the transverse motions are slow compared with the velocity in the beam direction, it is possible to substitute the transverse linear momenta $m\,dx/dt$ and $m\,dy/dt$ by the tangent values $x' = dx/dz$ and $y' = dy/dz$ of the divergence angles for all the individual trajectories. Thus the commonly used two-dimensional emittance definitions regard the patterns that the particles independently occupy in the (x, x') and (y, y') planes.

If the electron trajectories are closely paraxial, the transverse phase space area $A(x, x')$ and $A(y, y')$ are constant quantities. This area, unless a factor π, is known as the beam emittance ε.

The transverse phase space *XX'* is, therefore, the plane where lie the points (x, x'), where x is the position along the transverse axis, while x' is the angular spread value of the singular beam trajectory in this point. The resulting pattern is quite frequently of elliptical shape (fig. 1.8).

The units to measure emittances, according to a frequently used convention, are [π mm mrad].

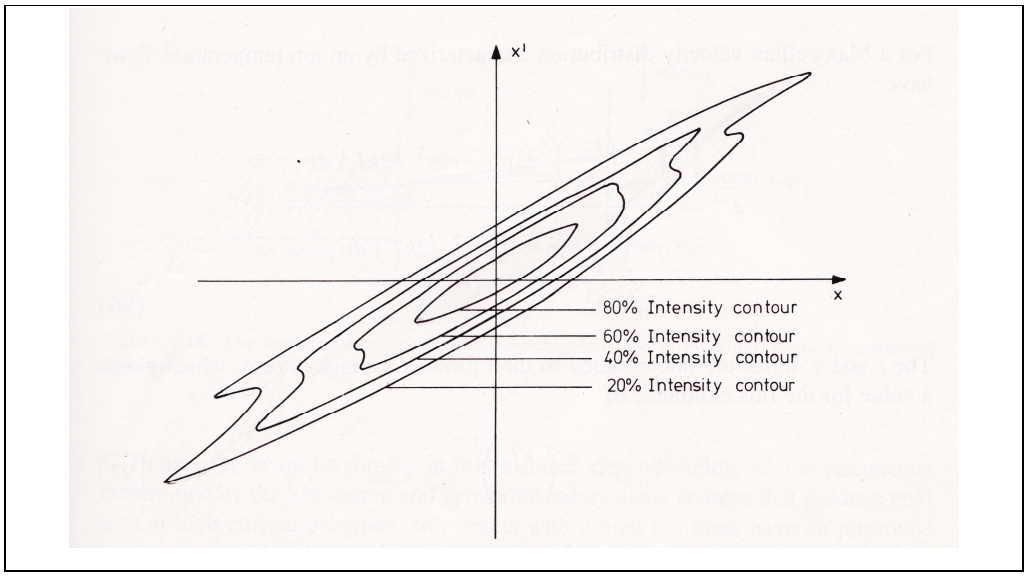

Figure 1.8 – Transverse emittance diagram with the contours of equal intensity.

Very frequently, the beam has a non-uniform density and it is useful to introduce the concept of the fraction of all the particles that lie inside the area whose contour is a line of equal density. In the case of a Gaussian beam profile, derived from a common thermal ion distribution, the beam emittance area ε which contains a fraction f of all beam ions is related to f by the expression

$$f = 1 - \exp\left(\frac{-\varepsilon}{2\varepsilon_{rms}}\right) \tag{1.42}$$

where ε_{rms} is the root mean square emittance statistically defined by Lapostolle [17]

$$\varepsilon_{rms} = \sqrt{\overline{x^2}\,\overline{x'^2} - (\overline{xx'})^2} \tag{1.43}$$

where the averages for x and x' are weighted by the beam intensity.

For a uniform ion beam with circular spot of radius *r* has been found that [18]:

$$\varepsilon_{rms} = \frac{r}{2}\sqrt{\frac{kT}{mv_b^2}} \tag{1.44}$$

for a simply thermionic emission, while

$$\varepsilon_{rms} = \frac{r}{2}\sqrt{\frac{nh\nu - \phi}{mv_b^2}} \tag{1.45}$$

for photo-emission process at the *n*-photon order. In the above expressions v_b is the particles velocity parallel to the beam axis. The normalized-relativistic emittance is defined by means of

$$\varepsilon_{N\,rms} = \gamma\beta\varepsilon_{rms} \tag{1.46}$$

where $\gamma = \frac{1}{\sqrt{1-\left(\frac{v^2}{c^2}\right)}}$ and $\beta = \frac{v}{c}$ are the relativistic coefficients.

By substituting in the above expression, it is possible to obtain

$$\varepsilon_{N\,rms} = \gamma\frac{r}{2}\sqrt{\frac{nh\nu - \phi}{mc^2}} \tag{1.47}.$$

To measure the angle of a trajectory precisely a two-slit approach [19] is used in all diagnostics; this is shown conceptually in Fig. 1.9. The position of the front slit

determines the spatial position of the particles, while the rear slit measures the angle and the angular spread of the trajectories passing through the front slit.

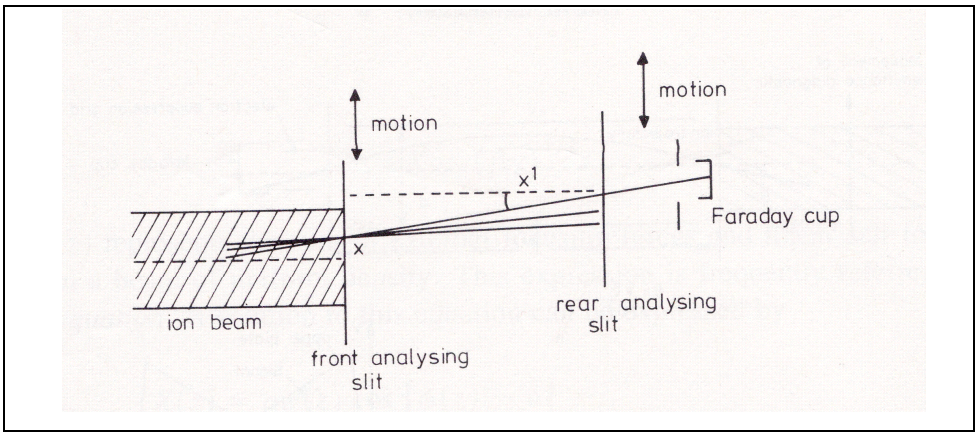

Figure 1.9 – Two-slit approach to evaluate emittance as measurement of position and angle separately.

The emittance is closely related to the concept of beam *brightness*, which contains together intensity I_b and angular dispersion ε of a particle beam, it is usually defined as [18]

$$B = \frac{I_b}{\pi^2 \varepsilon_{xrms} \varepsilon_{yrms}} \tag{1.48}.$$

The normalized brightness is more useful and is defined as

$$B_n = \frac{I_b}{\pi^2 \varepsilon_{nxrms} \varepsilon_{nyrms}} \tag{1.49}.$$

References Chapter 1

[1] C. Kittel, "*Introduction to solid state physics*", Wiley, (1968).

[2] S. Dushman, "*Electron Emission from Metals as a Function of Temperature*", Phys.Rev. **21**, 623 (1923).

[3] D. J. Griffiths, "*Introduction to Electrodynamics"*, Prentice Hall (1998).

[4] X. Wang, "*Emission of prompt electrons during excimer laser ablation of aluminium targets*", Appl. Phys. Lett. **75**, 7 (1999).

[5] R.H. Fowler and L.W. Nordheim, "*Electron emission in intense Electric fields*" Proc. Roy. Soc. (London), Ser A 119, 173 (1929).

[6] R. H. Good, Jr., and E.W. Muller, "*Handbuch der Physik*", Vol. 21, Springer, Berlin (1956).

[7] W.W. Dolan, W.P. Dyke and S.K. Trolan, "*The Field Emission Initiated Vacuum Arc. II. The Resistively Heated Emitter*", Physik. Rev. **91**, 1054 (1953).

[8] S.P. Bugaev, E.A. Litvinov, G.A. Mesyats and D. J. Proskuroskii, "*Explosive emission of electrons (from a cathode) "*, Sov. Phys. Usp. **18**, 51 (1975).

[9] A. Beloglazov, V. Nassisi and M. Primavera, "*Excimer laser induced electron beams on an AI target: Plasma effect in a 'nonplasma' regime*", Rev. Sci. Instrum. **66,** 7 (1995).

[10] R.H. Fowler and Guggenheim, "*Statistical Thermodinamics*", Cambrige University Press (1965).

[11] R.H. Fowler, "*Statistical Mechanics*", University Press (1966).

[12] A.H. Sommer, "*Photoemissive materials*", Wiley & Sons (1968).

[13] D.J. Leopold, J.H. Buckley, P. Rebillot, J. App. Phys. 98, 043525, 1-5 (2005).

[14] J. Lin and T.F. George, "*Laser-generated electron emission from surfaces: Effect of the pulse shape on temperature and transient phenomena*", J. Appl. Phys. **54**, 382 (1983).

[15] J.H. Bechtel, W. Lee Smith, N. Bloembergen, Phys. Rev. **B 15,** 4557 (1977).

[16] E.M. Logothesis and P. Hartman, "*Three-photon photoelectric effect in gold*", *Phys. Rev. Lett.* **18**, 581 (1976).

[17] P. Lapostolle, IEEE Trans. Nucl. Sci. **NS 18**, 1101 (1971).

[18] I. G. Brown, *"The Physics and Technology of ion Sources"*, Wiley & S. (1989).

[19] A. Van Steenbergen, IEEE Trans. Nucl. Sci. **NS 12**, 746 (1965).

2 Experimental apparatus

2.1 Introduction

In this chapter the experimental equipment used in the work will be pointed up and explained in details: the vacuum chamber, the targets, the diagnostic system, and the way to record the laser and current pulses. Complete description of the characteristics of excimer lasers will be performed: the focus will be towards the active medium, the laser camera, the pumping systems used, the duration and the shape of the laser pulses. The whole experimental apparatus was realized in the Applied Electronics Laboratory LEAS of the Department of Physics in Lecce.

2.2 Experimental set-up description

The devices used in this work are shown in figure 2.1 and schematically represented in figure 2.2.

The used sources were three different wavelength excimer UV lasers. The first laser was a KrF operating at 248 nm and 5 eV photon energy; it was an commercial pulsed laser (Lambda physics COMPex 205) with pulse duration (FWHM) of about 23 ns. The second one was a XeCl operating at 308 nm and 4.02 eV photon energy; it was a home-made pulsed laser with pulse duration at FWHM of about 16 ns. The third one was a KrCl operating at 222 nm and 5.6 eV photon energy; it was a home-made pulsed laser with pulse duration at FWHM of about 10 ns. These lasers work at irradiance range between 0.1 and 10 GW/cm^2.

The laser beam is led by a totally reflective aluminated mirror (M), towards a support on which are placed same neutral filters (F) that have the function to vary the light intensity.

The beam is then directed towards a convergent lens (L), of focal f =1 m, that focuses the rays, with an incident angle of 0^o, on the target (T) for electron generation, into the extraction chamber.

Between the filters and the lens is placed a beam splitter that deviates a portion of the laser beam on a fast photodiode (Ph) Hamamatsu R1328U-02, which allows to use the signal like a trigger and to record the temporal trend of the laser pulses directly on a digital oscilloscope.

All the devices are positioned onto metal rail in order to allow a better alignment of the laser beam.

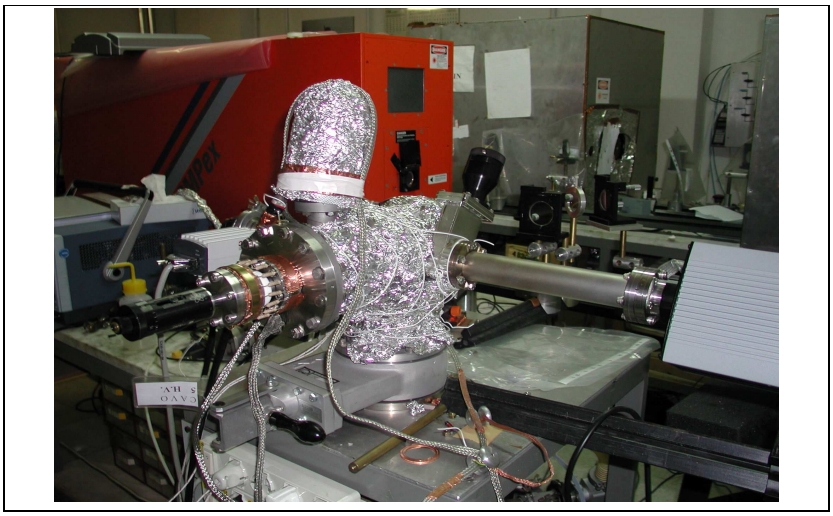

Figure 2.1 – Photo of the experimental apparatus.

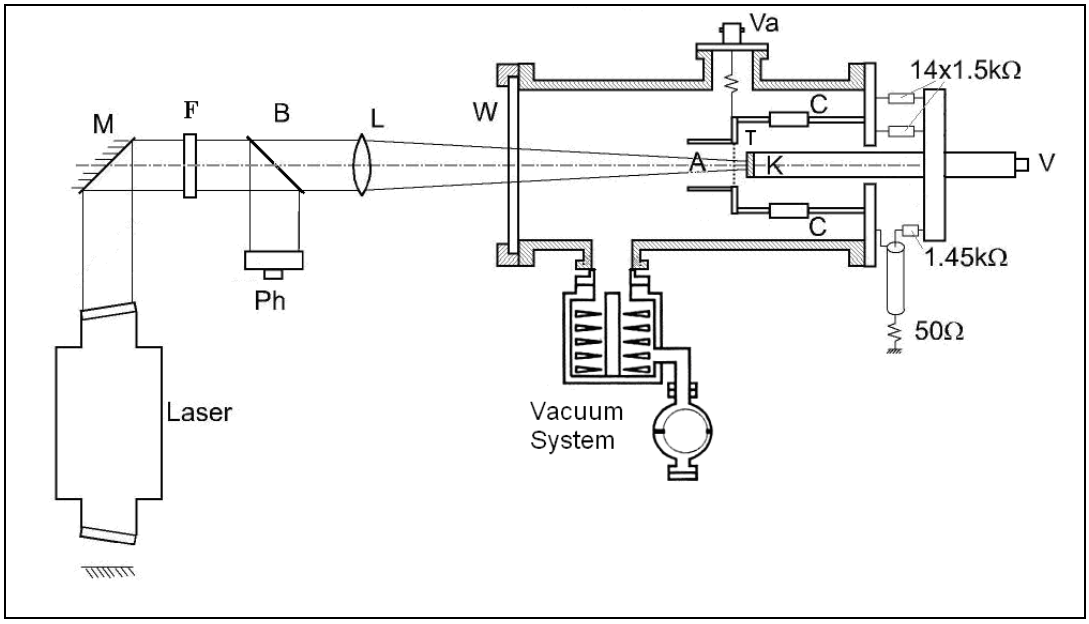

Figure 2.2 – Scheme of the experimental apparatus. M: totally reflective mirror, Ph: photodiode, B: beamsplitter, W: quartz window, F: crystal filters, L: convergent lens. A: anode, T: target, K: sample-holder, Va: high voltage. C: capacitor.

2.2.1 Extracting chamber

The electron extraction was performed inside of a vacuum stainless-steel chamber with cylindrical structure. High vacuum level was obtained by means of a rotary pump and a turbo-molecular pump (VARIAN) connected through a butterfly valve to the chamber; by using this system with heater bands, a work vacuum level of the order of 10^{-5} - 10^{-6} Pa was reached. INFICON quadrupole mass spectrometer was connected by insulating flange to the chamber (figure 2.1), in order to control the quality of the vacuum and the residual gases present in the chamber. Picking up the signal of the load resistor by a digital oscilloscope Le Croy Wavepro 7100 (1 GHz, 20 GS/s) the electron waveform was recorded.

In order to allow the laser-beam to reach the target, a quartz window (W) was used to close the chamber. On the back an insulating flange connected to a metallic cylinder with the function of target holder and cathode (K), was present. The anode (A), included in an empty cylinder, was made of a stainless steel grid with 4 meshes per mm^2, called *accelerating grid*. This one had an optical transmittance of 64%, experimentally evaluated; it allowed the laser beam to illuminate the cathode. The system containing the grid was held to positive potential on respect to ground and his function is to accelerate the photoelectron emitted from the target. Four capacitors (C) of 350 pF/40 kV, called *buffer* capacitors, were applied to the anode and connected in parallel to the generator which supplies the accelerating voltage. Their function was to stabilize the voltage value on the anode during the extraction. The maximum current provided from the power supply is very little (of the order of 10 mA), because it is

characterized by a high internal resistance. Therefore, during the fast current transient, when the laser beam interacts with the target, it could be happen that the output voltage is not constant. This problem is avoided by these capacitors, and the charge amount supplied in the accelerating phase is smaller than the one stored.

The extracted electrons were recorded in lower time than a nanosecond because of the coaxial structure of the interaction chamber as well as the acquiring system.

In order to evaluate the laser energy, a joulemeter Gentec ED-500, placed on the guide near the chamber gate, is used. The joulemeter is connected to an oscilloscope and the energy is measured by converting a voltage detection. The conversion factor depends on the wavelength range, because of the different absorption of the material that constitutes the device; for the used wavelengths the conversion factor V/J was 2.12 for KrF, 2.19 for XeCl, 2.03 for KrCl. The net energy incident on the target was obtained by considering the attenuation factor due to the grid and the quartz window, experimentally measured. This one depends, of course, on the utilizing wavelength; it was carried out a value of 52% for XeCl, 56% for KrF and 60 % for KrCl laser.

The sample-holder (K) was placed in a ring structure; an insulating flange isolated electrically it from the rest of the apparatus. The distance anode-cathode could be modified by using a screw cursor (V), present on the external part of the sample-holder (K), with a precision of 0.001 inches (corresponding to 0.0254 millimeters).

In order to record the genuine current pulses, the sample-holder (K) and the cursor (V) were ground-connected through a parallel of fifteen resistors, whose value was about 1500 Ω. In particular, one resistor of them was of 1450 Ω, connected in series to a 50 Ω coaxial cable.

These results carry out from a study that leads to consider the structure sample-holder like a transmission line of characteristic impedance 100 Ω. The device was used also like *resistive shunt* and it has the purpose to realize a radial symmetry for the signal propagation. In this way the system supplied a voltage detection at its terminals more uniform with respect to the taking point of the signal.

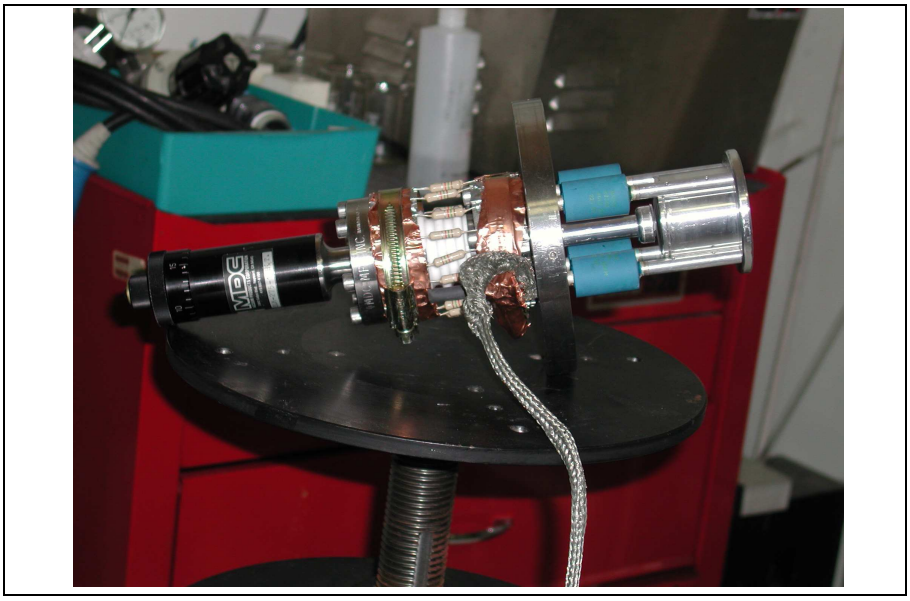

Figure 2.3 – Photo of the sample-holder with the resistive shunt.

The above mentioned coaxial cable was useful to the transmission of the signal, produced by the extracted electrons, to the digital oscilloscope.

The three sources used provided a laser spot of about 43 mm^2 for KrF, 52 mm^2 for XeCl and 72 mm^2 for KrCl.

The distance anode-cathode was set to 3.7 mm for Zn target and 5 mm for Y target; the maximum accelerating voltage applied was 25 kV. The application of

higher voltage values was limited for the presence of electric arcs in the accelerating gap. The work function was 4.33 eV for zinc and 3.10 eV for yttrium cathode.

2.2.2 Cathode characteristics

In the present experimental work two different metallic materials were used to realize the cathodes: zinc and yttrium. They were two disks in shape, having 2 cm of diameter and 0.5 mm of thickness; they were fixed on the sample-holder. The target diameter matched the sample-holder one and it has been attached at the stem by using silver paste.

The Zn cathode surface has been smoothed by grinder/polisher machine and then treated by ultrasounds bath, in order to remove possible superficial impurities. After, it has been placed on the stem, inside the vacuum chamber. The incidence angle of the laser beam on the target surface was fixed for all the measurements at 0°.

Two Y bulks with different surface morphologies were realized by utilizing grinder and sand-blasting machines: smooth and rough. The purpose is to study the variations of the electron emission efficiency due to the modification, induced or natural, of the cathode surface.

In the table 2.1 and 2.2 the main characteristics chemical-physical of the zinc and yttrium, respectively, are reported.

Chemical Symbol	Zn
Atomic Number	30
Electron Configuration	[Ar] $3d^{10}4s^2$
Work Function	4.33 eV
Boiling Point	1180 K
Melting Point	693 K
Electrical Resistivity (at 300 K)	5.964 μΩcm
Specific Heat Capacity (at 25 °C)	388 J/(kg·K)
Density (at 25 °C)	7140 kg/m^3
Thermal Conductivity (at 27 °C)	116 W/(m·K)
Reflectivity (for λ = 222÷308 nm)	70÷80 %

Table 2.1 – Chemical-physical properties of the zinc.

Chemical Symbol	Y
Atomic Number	39
Electron Configuration	[Kr] $4d^15s^2$
Work Function	3.10 eV
Boiling Point	3609 K
Melting Point	1799 K
Electrical Resistivity (at 300 K)	5.96 μΩ·cm
Specific Heat Capacity (at 25 °C)	298 J/(kg·K)
Density (at 25 °C)	4470 kg/m^3
Thermal Conductivity (at 27 °C)	17.2 W/(m·K)
Reflectivity (for λ = 222÷308 nm)	60÷70 %

Table 2.2 – Chemical-physical properties of the yttrium.

To evaluate the average surface roughness the following expression has been used [1]:

$$z = a\left(1+\sin\frac{2\pi}{b}x\right) \qquad (2.1),$$

where a is the average half-amplitude of the periodic trend of the roughness profile recorded by the profilometer, while b is the average spatial periodicity. Therefore, it is possible to define the roughness as the ratio between the average value of a and b,

$$R_a = \frac{a}{b} \qquad (2.2).$$

For Zn and Y smooth samples, the average roughness coefficient R_a is of the order of 10^{-2}: despite the smoothing treatment, a certain roughness is present (fig. 2.4). For Y rough sample R_a is of the order of 10^{-1} (fig. 2.5).

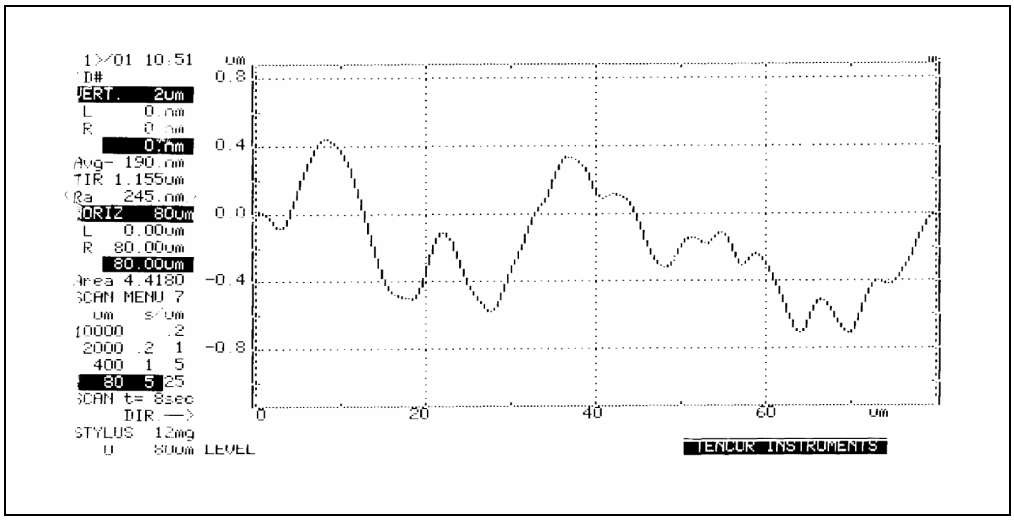

Figure 2.4 – Roughness profile plot for zinc cathode, carried out by profilometer.

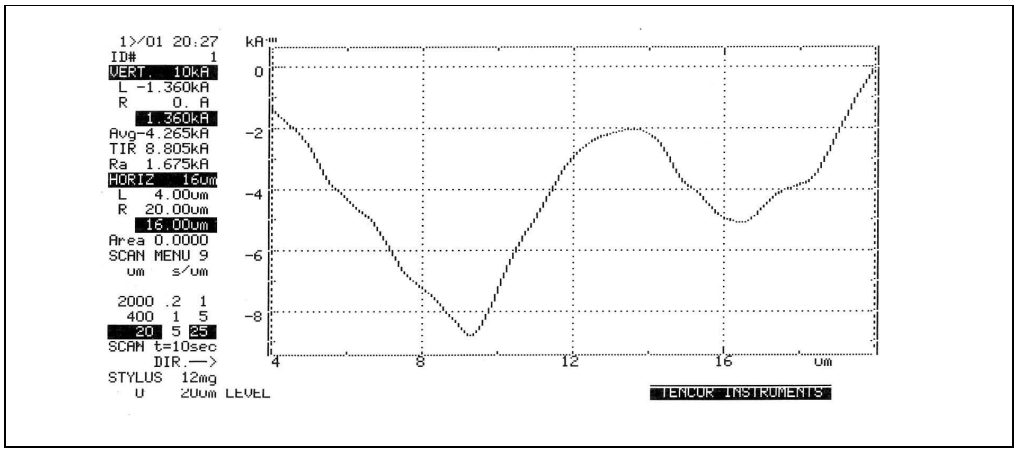

Figure 2.5 – Roughness performance of Y rough sample, carried out by profilometer.

2.2.3 Diagnostic system

The choice of the analysis device consists of an accurate diagnostic system, able to get what it is really measured.

An electron beam that spreads through the vacuum generates in the neighborhood a magnetic field that can interact with near conductor materials. Furthermore, if these ones have closed circuit it is possible to observe induced currents circulating inside them. On this principle is based the operation of Rogowski coil [2] and other devices, like magnetic loops [3]. It is noteworthy to remember that just these electromagnetic induction phenomena can perturb the experimental measurements. This problem can occur, almost, when the propagation structures of the signals don't hold a constant symmetry. Arise, in this way, the so-called spurious signals, produced by the inducted currents, which added themselves to the ones due to the electrons gathered into the

collector. The result is a single waveform on the oscilloscope and the measure is inevitably faked.

Due to the high attenuation factor of magnetic devices, in this thesis work, to perform the measurements, it was chosen an alternative analysis system: the resistive shunt [4]. This one is independent from possible electromagnetic induction phenomena. In order to verify the presence of a contribution due to the induced currents into the total signal read on the oscilloscope, a simulation device, schematized in figure 2.6, was built up. The calibration was accomplished simulating the electron beam by considering a current carrying in the cathode-holder rod.

To diagnose the electron beam it was necessary to consider the cathode-holder together with the various elements of the chamber, like a transmission line (figure 2.7). When the electrons leave the cathode, a positive pulse propagates towards the end of the rod. Nevertheless, being the rod long just 20 cm, a delay time more than 1 ns is observed. This result is due to the presence of buffer capacitors.

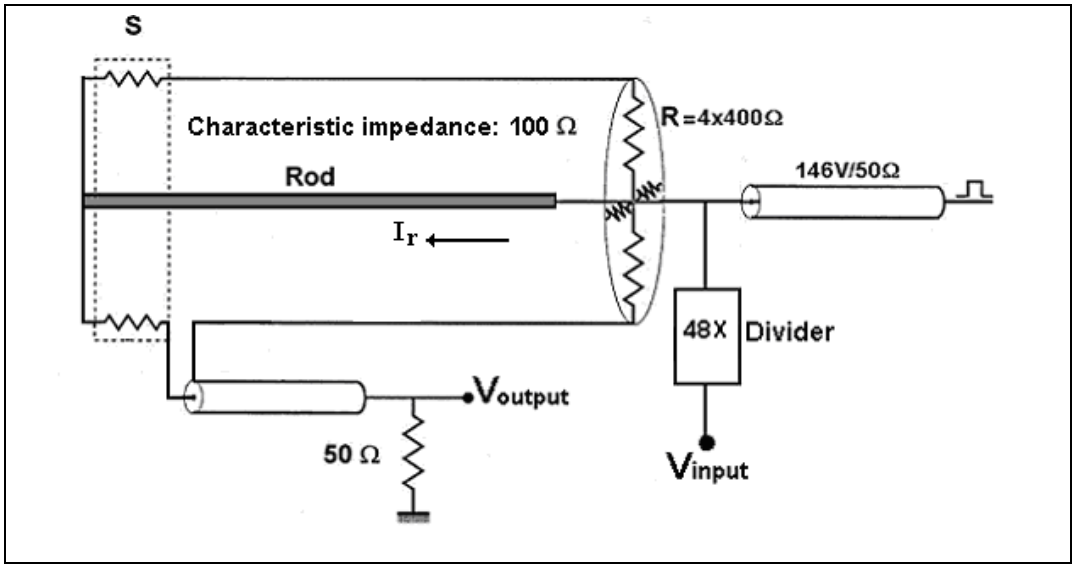

Figure 2.6 – Calibration system. S: resistive shunt.

In this case the characteristic impedance value is very difficult to determine. Even if the characteristic impedance for a transmission line is defined by the expression

$$R_0 = \sqrt{\frac{L}{C}} \qquad (2.3),$$

where L is the inductance and C is the capacity of the line, we determined it experimentally.

Theoretically we might consider the structure of the chamber like an internal conductor of 12 mm in diameter and more external conductors of different diameter with four capacitors inside. Approximating the system like a coaxial line, R_0 becomes

$$R_0 = \frac{1}{2\pi}\sqrt{\frac{\mu}{\varepsilon}}\ln\left(\frac{R}{r}\right) \qquad (2.4),$$

where ε is the dielectric constant, μ the magnetic permeability, R = 34 mm e r = 6 mm are the equivalent radii of the two conductors. In this case it was obtained a characteristic impedance R_0 of about 100 Ω, even experimentally.

Due to the 50 Ω output impedance of the pulse generator line used for the calibration, 4 resistors of 400 Ω were connected in parallel between the cathode entrance and the ground, as to obtain exactly 100 Ω (figure 2.6) and to avoid signal reflections.

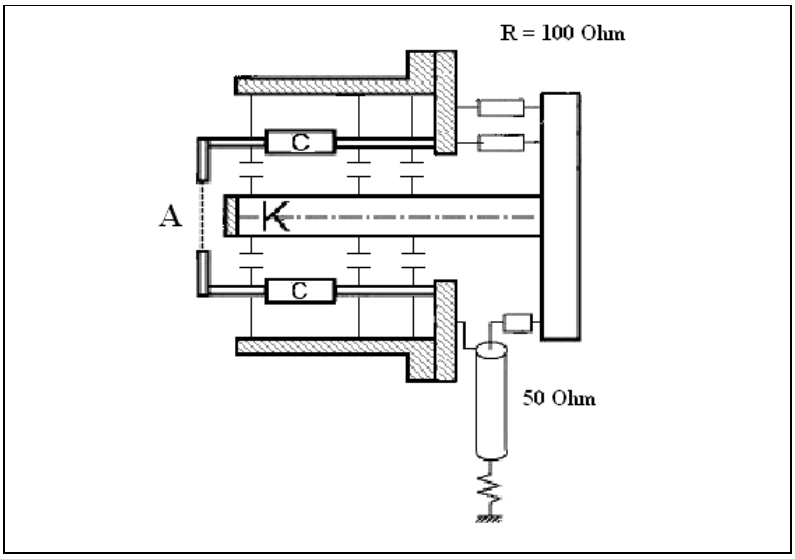

Figure 2.7 – Scheme of the cathode stem and the chamber walls like transmission line.

The input voltage V_{input} was 154 V in amplitude, that generates a current pulse into the cathode of 1.54 A. By utilizing the output signal value V_{output} = 5.5 V, it was possible to estimate experimentally the *attenuation factor*

$$\kappa = \frac{I_{cathode}}{V_{output}} \qquad (2.5).$$

From the figure 2.6, V_{input} = (3.2 x 48) V $\approx$ 154 V, where "48" is the reduction factor of the divider used to measure the input voltage. Therefore

$$I_{cathode} = \frac{154\ V}{100\ \Omega} = 1.54\ \text{A}. \qquad (2.6).$$

It was obtained an attenuation factor

$$\kappa = \frac{1.54\ A}{5.5\ V} = 0.28\ \frac{\text{A}}{\text{V}} \qquad (2.7).$$

The figure 2.8 shows the calibration waveforms. From the plots it is possible to observe that, really, the output pulse is similar to the input one, the only difference being the pulse amplitude. It is noteworthy that the rise-time and the fall-time were the same for both the signals. During the experimental work the calibration of the shunt was usually controlled.

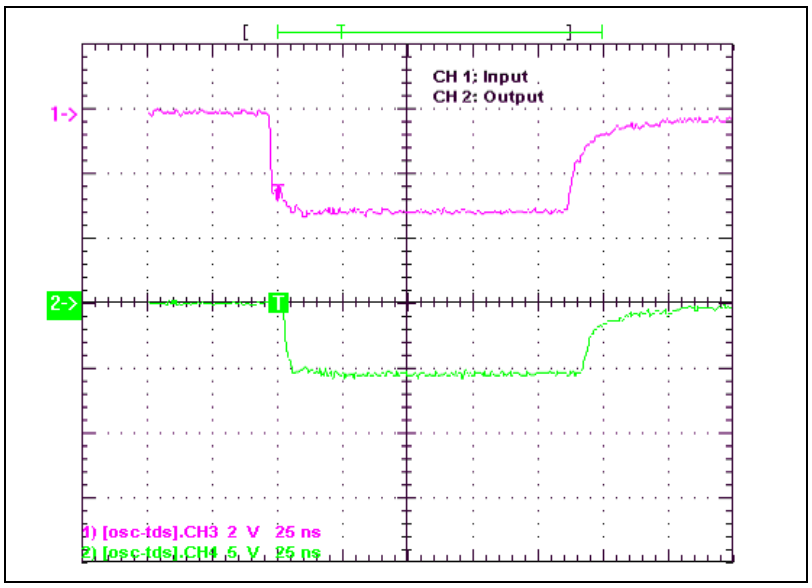

Figure 2.8 - CH1 input signal; CH2 output signal.

2.3 The excimer lasers

The excimer lasers represent a very interesting and important class of coherent radiation sources that uses the transitions between different electron states of special molecules called “excimers”.

These ones use like active medium a gas whose molecules are composed by halogen atoms (F, Cl, Br,…) and noble gas atoms (Xe, Kr, Ar,…). The noble gas ground state has the electron configuration $s^2 p^6$, while the first excited state has the configuration $s^2 p^5 s$, like the ground state of the alkaline atoms (Li, Na, K,…). As for the alkaline, therefore, also the excited noble gas atoms are highly electropositive, inducing the formation of ionic bond with electronegative elements like the halogens. The term "excimer" is acronym of the words "excited dimer" and it indicates the diatomic molecules that present a bond state only in the excited electron levels, while they are dissociated in the ground level.

In the mixture used for the laser operation there is also a *buffer* gas (usually *He* or *Ne*). This one has the double function to absorbing the pumping energy and to transfer it to the excimer molecules. The figure 2.9 shows the energy levels diagram of the excimer molecule.

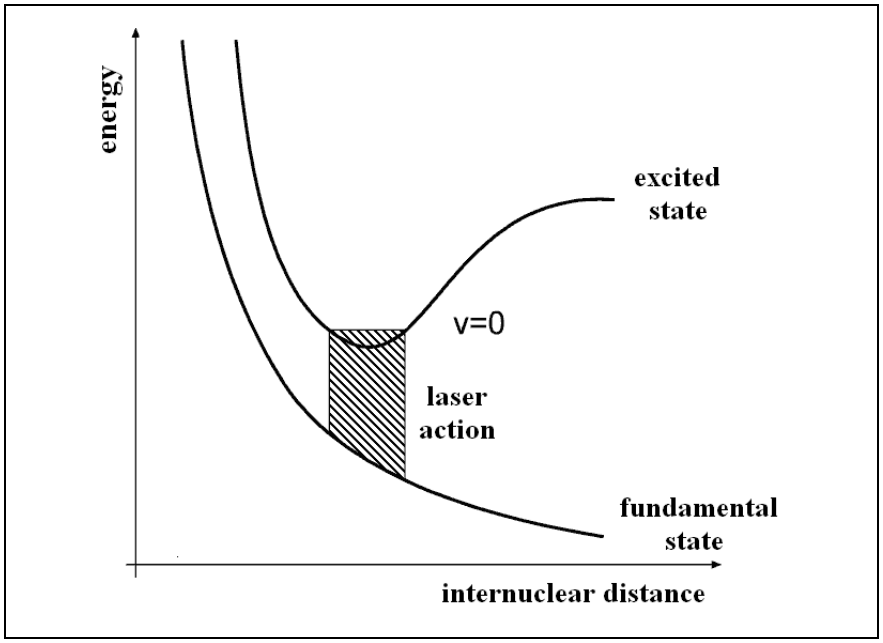

Figure 2.9 – Electron states of excimer molecule.

There are several ways to pump energy into the system for the population inversion of the electron levels of the excimer molecule. For the laser systems used in this work, the pumping method used is the capacitive discharge (figure 2.10).

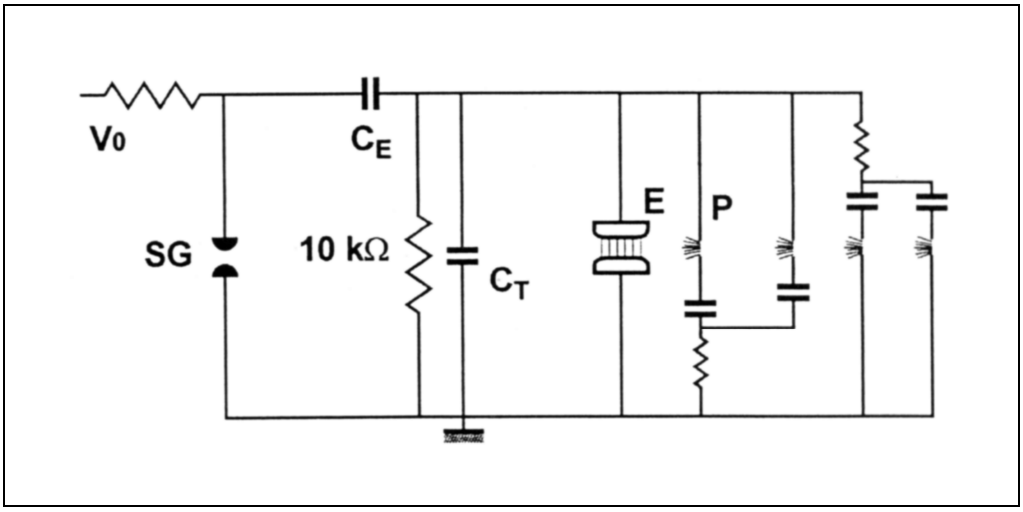

Figure 2.10 – Typical operating scheme for excimer laser: **SG** spark gap; $\mathbf{C_E}$ capacitor; $\mathbf{C_T}$ breakdown ceramic capacitors; **E** electrodes; **P** preionizators; $\mathbf{V_0}$ voltage supply.

Practically, there is a electrode couple (*E*) few tens of centimeters long, connected in parallel with a series of high voltage ceramic capacitors (C_T), inside the laser mixture and, therefore, inside the chamber. By means a fast high voltage switch (spark-gap) the ceramic capacitors were charged by a capacitor (C_E), connected to the power supply.

2.3.1 The KrF laser

The KrF laser is one of the most important in the categories of excimer lasers. The laser KrF emits at 248 nm wavelength, corresponding to 5.0 eV single photon energy; the pulse duration at full-width-half-maximum (FWHM) is about 23 ns.

The two main reaction mechanisms, responsible for the production of the molecule *KrF*, carried out from the excitation of the atoms *Kr* or Kr^+. The first process was described by using the following expressions

$$e + Kr \rightarrow e + Kr^*$$
$$Kr^* + F_2 \rightarrow (KrF)^* + F$$

where *Kr* was, at first, excited by a discharge, while after it reacts with a fluorite molecule.

The second process can be illustrated by means of the following three reactions

$$e + Kr \rightarrow 2e + Kr^+$$
$$e + F_2 \rightarrow F^- + F$$
$$F^- + Kr^+ + M \rightarrow (KrF)^* + M$$

First ions *Kr* and *F* were produced, and after they recombined themselves at the presence of a *buffer* gas *M*, in this case Ne.

In this work, it was used a mixture composed by

Kr	⇒	4 %
F_2	⇒	0.1 %
He	⇒	1.9 %
Ne	⇒	94 %

2.3.2 The XeCl laser

The laser XeCl emits at 308 nm wavelength, corresponding to 4.02 eV single photon energy; the pulse duration at FWHM is about 16 ns. For this laser type, the active medium was composed by a mixture of the noble gas Xe, the halogen Cl, and the buffer Ne, at about 3 atm of total pressure. Due to the discharge, several chemical-physical reactions begin inside the gas mixture which lead to the excimer formation. The operating characteristic, as the reactions for $XeCl^*$ formation, are the same own of the KrF laser. There are, also in this case, two formation channels. The ionic channel, through the reactions

$$HCl + e^- \rightarrow H^+ + Cl^- + e^- \Rightarrow \text{dissociation of HCl}$$

$$Xe + e^- \rightarrow Xe^* + e^- \Rightarrow \text{excitation of Xe}$$

$$Xe + e^- \rightarrow Xe^+ + 2e^- \Rightarrow \text{ionization of Xe}$$

$$Xe^+ + Cl^- + Ne \rightarrow XeCl^* + Ne \Rightarrow \text{formation of } XeCl^*$$

and the neutral channel

$$Xe^{*} + HCl + Ne \rightarrow XeCl^{*} + H + Ne.$$

In this work, it was used a mixture composed by

Xe	⇒	2 %
HCl	⇒	0.2 %
He	⇒	2.8 %
Ne	⇒	95 %

2.3.3 The KrCl laser

The laser KrCl emits at 222 nm wavelength, corresponding to 5.6 eV single photon energy; the pulse duration at FWHM is about 10 ns. This is the highest photon energy used. For this laser type, the active medium was composed by a mixture of the noble gas Kr, the halogen Cl, and the buffer Ne, at about 3 atm of total absolute pressure. Due to the discharge, chemical-physical reactions, which lead to the excimer formation, begin inside the gas mixture. The operating characteristic, as the reactions for $KrCl^{*}$ formation, are the same seen for the KrF and XeCl laser. There are, also in this case, two formation channels. The ionic channel, through the reactions

$$HCl + e^- \rightarrow H^+ + Cl^- + e^- \Rightarrow \text{dissociation of HCl}$$

$$Kr + e^- \rightarrow Kr^* + e^- \Rightarrow \text{excitation of Kr}$$

$$Kr + e^- \rightarrow Kr^+ + 2e^- \Rightarrow \text{ionization of Kr}$$

$$Kr^+ + Cl^- + Ne \rightarrow KrCl^* + Ne \Rightarrow \text{formation of } KrCl^*$$

and the neutral channel

$$Kr^* + HCl + Ne \rightarrow KrCl^* + H + Ne.$$

In this experimental work, it was used a mixture composed by

$$Kr \Rightarrow 11\ \%$$

$$HCl \Rightarrow 5\ \%$$

$$He \Rightarrow 5\ \%$$

$$Ne \Rightarrow 79\ \%$$

References Chapter 2

[1] V. Nassisi and M. R. Perrone, *"Generation and characterization of high intensity electron beams generated from rough photocathodes"*, Rev. Sci. Instrum. **70,** 11 (1999).

[2] V. Nassisi and A. Luches, "*Rogowski coils: teory and experimental risults*", Rev. Sci. Instrum. **50,** 900 (1979).

[3] R. L. Copeland, J. L. Adamski, W. O. Doggett, D. L. Morrow, W. H. Bennet, "*Nanosecond response gasket-type magnetic loop current monitor for relativistic electron beam current measurements"*, Rev. Sci. Instrum., **50**, 233 (1979).

[4] L. Martina, V. Nassisi, A. Pedone, P.P. Pompa and G. Raganato, "S*tudies of electron beams propagation in space-charge regime*", Rev. Sci. Instrum., **73**, 2552 (2002).

3 Experimental results and analyses

3.1 Introduction

In this work the incidence of the experimental parameters on the electron emission from metal targets, irradiated by excimer lasers, was analyzed. The incident energy and the charge accelerating voltage were varied during the experiments. The surface morphology, induced or natural, of the samples was studied, because it was found that the charge yield increased with the superficial irregularity of the target. Therefore, micro-structured defects were experimentally created on the cathodes and its effects on electron beam studied in detail.

In this chapter are reported the experimental results and the analyses of the measurements performed on all the photoemitted electron beams.

3.2 Measurements with Zn cathode

In this experimental phase the analyzed cathode was a Zn bulk with smooth surface. For all the measures the anode-cathode distance was fixed at 3.7 mm and the maximum applied accelerating voltage was 25 kV, limited by the presence of arcs in the anode-cathode gap. The cathode work function was 4.33 eV. The pulsed laser-induced photoelectric charge was measured as a function of the voltage applied between anode and cathode. In this work the measurements were performed after to have operated the vacuum into the chamber for almost two days.

The experiments were performed by using XeCl and KrF laser sources.

3.2.1 Data and analyses with XeCl laser

The XeCl photon had not sufficient energy to carry a conduction electron over the potential barrier placed on the target surface. During the experiment, besides, the sample reached the maximum temperature of about 500 K, so it is possible to neglect the thermionic contribute. Therefore it was supposed that the electron extraction is due mainly to the one and two photon absorption. From the Fowler-DuBridge equation (1.34) carried out the current density for XeCl laser

$$J_{XeCl}(t) \cong a_1^{XeCl} AT^2 I(1-R)\exp\left(\frac{h\nu-\phi}{kT}\right) + a_2^{XeCl} AI^2T^2(1-R)^2\left[\frac{1}{2}\left(\frac{2h\nu-\phi}{kT}\right)^2 + \frac{\pi^2}{6}\right] \qquad (3.1),$$

where the thermionic term was ignored.

In the figure 3.1 the performance of the photo-emitted peak current depending on the accelerating voltage, at three different laser energies incident on cathode, was plotted. The maximum current value was 2.3 A, obtained at 48 mJ energy and 12 kV accelerating voltage. This last was limited, because of the formation of breakdowns between anode and cathode. From the plot it is evident that the current obtained at 11 mJ reached the saturation regime already at 2 kV. At higher energy values, the saturation plateau is not clear; in fact the photoemission efficiency increases with the accelerating voltage. This behavior, called *linear regime*, can be considered like a result of the overlapping between the Schottky effect and the saturation one.

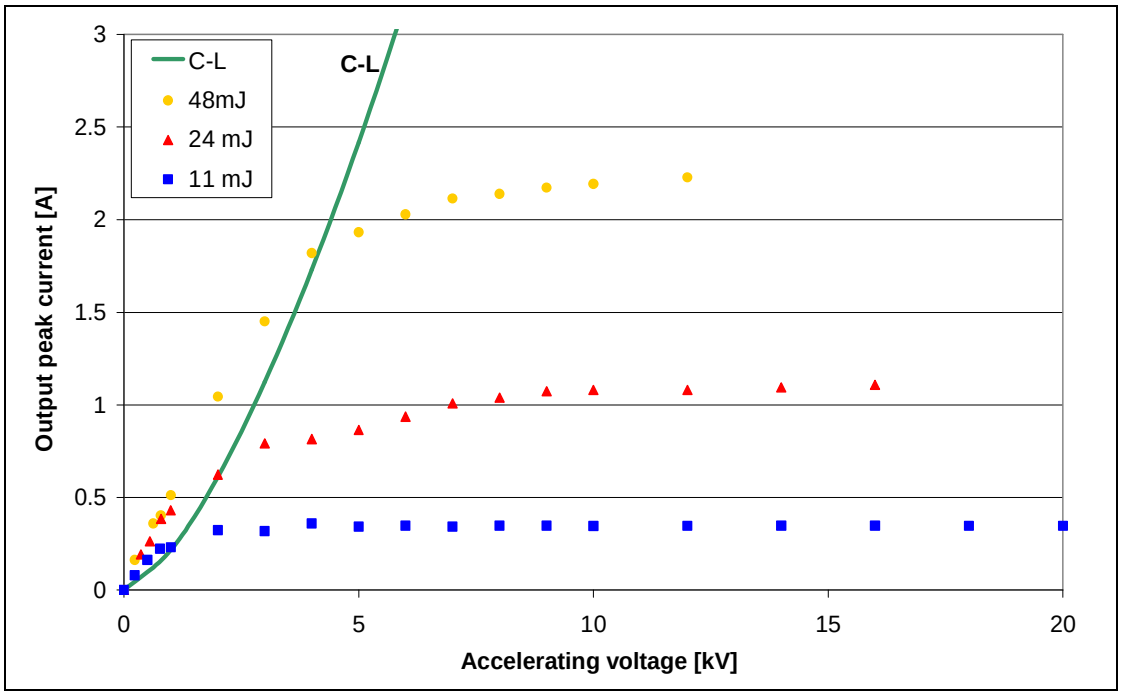

Figure 3.1 – Performance of the peak current vs. the accelerating voltage for Zn cathode irradiated by XeCl laser. C-L: Child Langmuir law.

The C-L curve in the plot represents the Child–Langmuir law for the studied system. It gave the limit of maximum current, in *space-charge regime*, correlated with a certain voltage and gap distance for an ideal diode

$$J_{CL} = 2.34 \cdot 10^{-6} \cdot \frac{V^{3/2}}{d^2} \qquad (3.2),$$

where S is the laser spot area, V is the accelerating voltage and d is the anode-cathode distance.

It was noteworthy to observe that in linear regime the slope of the current curve increases together to the laser energies and at low voltages the Child-Langmuir law (C-L curve) is violated (the experimental data overcome the theoretical maximum current). This fact was explained by considering the system not ideal: the cathode was not perfectly smooth and the anode was a grid. Both characteristics enhanced the electric field on the cathode surface and, as a consequence, its work function decreases. Due to the Schottky effect, in fact, the work function varies, in agreement with the following expression:

$$\phi = \phi_0 - \sqrt{\frac{e}{4\pi\varepsilon_0}}\sqrt{\beta E} \qquad (3.3),$$

where ϕ_0 is the zero field work function, E is the electric field strength, $(e/4\pi\varepsilon_0)^{1/2}$ is about $3.8\times10^{-5}\ N^{1/2}\ m\ C^{-1/2}$ and β is a constant that depends on the surface morphology. For a mirror-like surface $\beta = 1$, if this one, instead, begins to be irregular and to present imperfections $\beta > 1$. β, called the *electric field gain factor at the surface*, may be of the

order of $10^2 - 10^3$ for superficial whisker-like micro protrusions [1]. Therefore, considering the function (3.1), the current density can increase on the applied voltage and this fact explains the slope of the curves.

From figure 3.1 it was evident that the slope of the different curves grew with the laser energy and at low accelerating voltages the experimental data violated the Child-Langmuir law. This comportment was emphasized for higher laser energy and could be explained by considering the plasma formation on the cathode surface. The plasma, in fact, introduces a certain impedance in the anode-cathode region, shifting the Child-Langmuir law [2, 3]. Besides, from studies about the ion generation, it is well known that the plasma expand and this fact can shorten the anode-cathode distance [4]. As a consequence, the increase of the output current modifies the Child-Langmuir law in space-charge regime

$$J_{CL} = 2.34 \cdot 10^{-6} \cdot \frac{(V - ZI)^{3/2}}{(d - vt)^2} \qquad (3.4),$$

where V is the applied accelerating voltage, d is the anode-cathode distance, while Z and v are, respectively, the impedance and the expansion velocity of the plasma.

In the figure 3.2 the waveforms of the laser (upper trace) and current pulse (lower trace), at 11 mJ laser energy and 6 kV of applied voltage, are reported.

It is possible to note that the photoemitted current pulse presents a width lower than the laser one. This behaviour is typical of two-photon process: in this case, in fact, the current density depends on I^2 and this fact involved a FWHM decrease of about 4 ns for the current pulse.

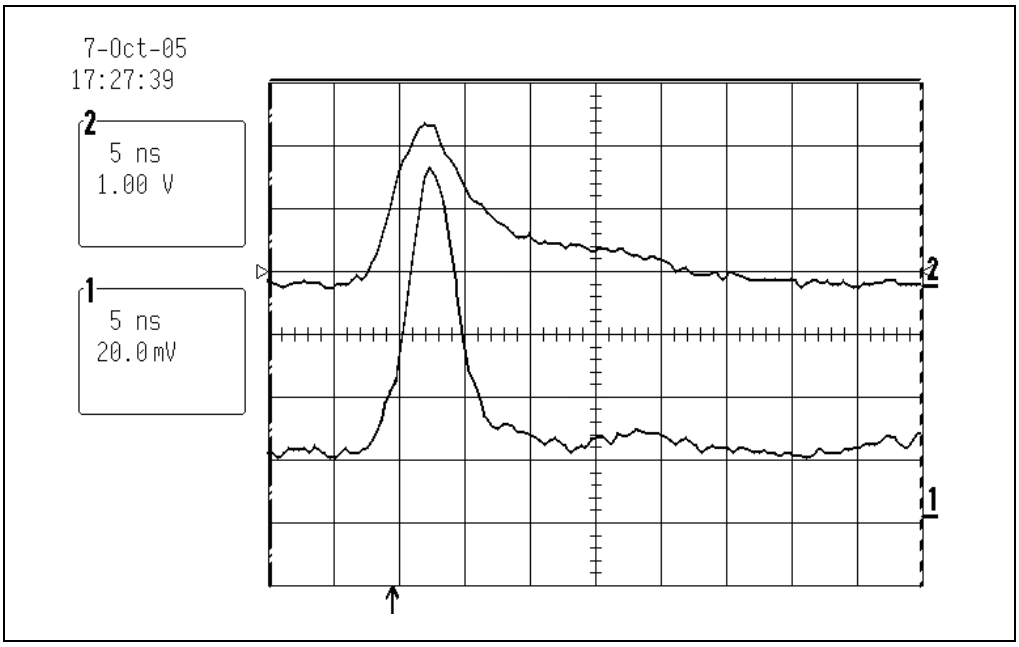

Figure 3.2 - Waveforms of laser (upper trace) and current pulse (lower trace) for laser XeCl, at 48 mJ laser energy and 12 kV applied voltage.

From this picture is evident, besides, that the current time duration is shorter than the laser one and it has an onset time delayed of about 2 ns. At higher incident laser energies, the process starts into the domain of the two-photon emission, but after the peak of laser intensity the electron emission increases. This enhancement is ascribed to the plasma formation that, apart from the decrease of the distance anode-cathode, can contribute to extract electrons. This behavior is evident in fig. 3.4, where the normalized curves of laser-intensity and photoemitted current on time, at 48 mJ energy and 9 kV applied voltage, are shown. The triangular points represent the temporal quantum efficiency (TQE), defined by the ratio between the number of extracted electrons and the number of incident photons at the *t* instant

$$\eta_{TQE}(t) = \frac{J(t)h\nu}{eI(t)} \qquad (3.5),$$

where $h\upsilon$ is expressed in eV, while $J(t)$ and $I(t)$ are the output current density and the incident laser intensity, respectively. In the present experiments the efficiency was practically calculated by means of the oscilloscope waveforms (fig. 3.3), utilizing the expression

$$\eta_{TQE}(t) = \frac{V_{el}(t) \cdot h\nu \cdot \kappa \cdot \int_0^{\infty} V_{ph}(t) \cdot dt}{V_{ph}(t) \cdot E_{laser}} \qquad (3.6),$$

where $V_{el}(t)$ is the amplitude, at the t instant, of the voltage signal on the oscilloscope screen due to the electron current, $V_{ph}(t)$ is the amplitude, at the t instant, of the voltage signal on the oscilloscope screen due to the incident photons, E_{laser} is the total incident laser energy and κ is the attenuation factor (2.7).

In this case, the quantum efficiency reached its maximum value close to 12 ns from the laser onset time. It was approximately 4.5×10^{-6}, obtained at 48 mJ laser energy and 9 kV accelerating voltage.

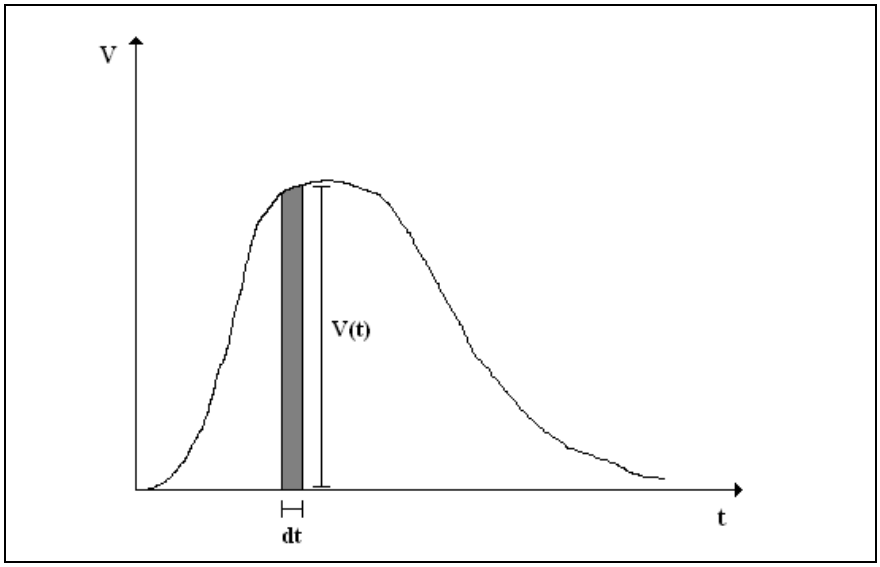

Figure 3.3 – Temporal quantum efficiency calculation by using oscilloscope signals.

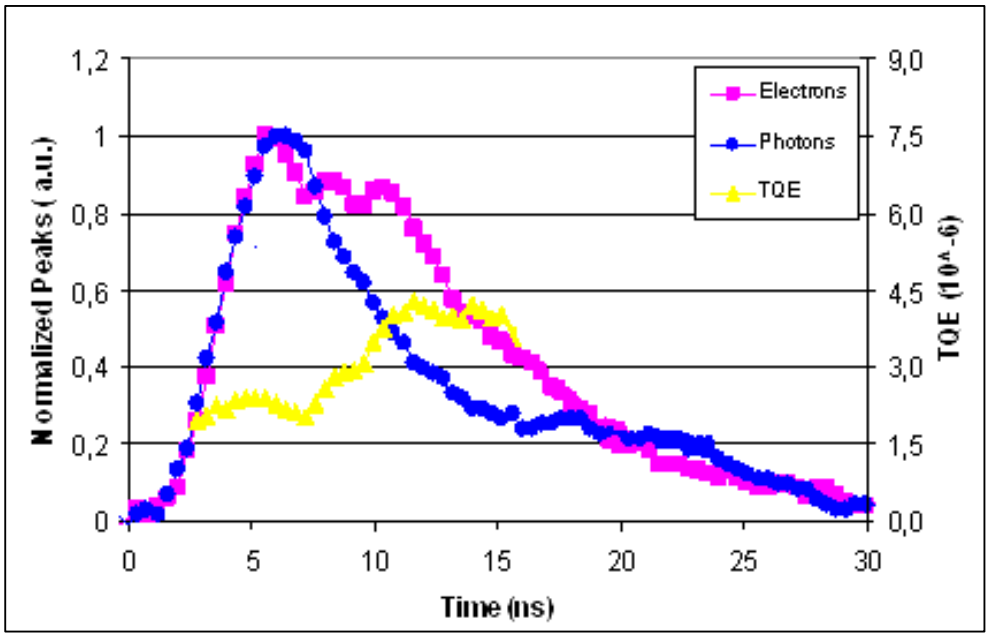

Figure 3.4 – Zn sample: normalized laser (blue line) and current (violet line) pulses, obtained by using the XeCl laser at 48 mJ energy and 9 kV applied voltage. The yellow line represents the TQE calculated in the same conditions.

3.2.2 Data and analyses with KrF laser

The results obtained by using KrF laser are very similar to the ones carried out with XeCl laser, even if in this case the predominant phenomenon is the one-photon process. In fact, the KrF photon energy is higher than the work function of the used metal; as a consequence in equation (1.38) is N=0 and the electron photoemission is mainly studied by one-photon process. From expression (1.40) it is possible to obtain

$$J_{KrF} \cong a_1^{KrF} AI(t)(1-R)\times\frac{1}{2}\left(\frac{h\nu-\phi}{k}\right)^2 \qquad (3.7),$$

where the term $\frac{\pi^2}{6}$ is neglected, because it is little with respect to the other term.

By the theory, the most of the current is directly depending on the difference between the single photon energy and the work function. Figure 3.6 shows the peak current value as a function of the accelerating voltage, at different laser energies: it is possible to observe that the maximum value of the peak current was close to 12 A, at 14 mJ laser energy and 16 kV applied voltage.

Comparing the slope of the current curves with the ones obtained with XeCl at the same incident energy, one find that the KrF ones were larger. The found results mean that the photoemission process depends strongly on the output current, weakly from the laser energy. In this case more current is produced and the more and more plasma is generated.

Even in this case, as for XeCl laser, at low accelerating voltages (few thousands of volts), there are a violation of the Child-Langmuir law (fig. 3.5).

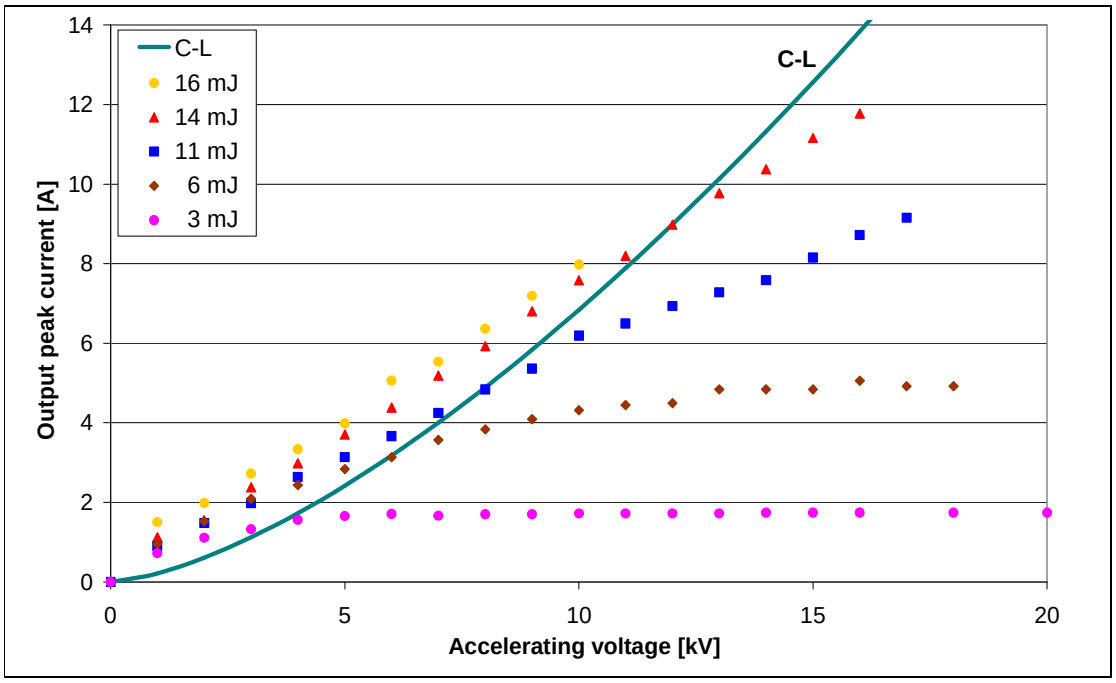

Figure 3.5 – Peak current vs. the applied voltage for Zn cathode irradiated by laser KrF.

The modification of the current limit was, in fact, caused by a geometrical change of the cathode surface. Since during its formation the plasma had a boundary velocity of about 34 km/s [2], under laser irradiation the anode-cathode distance shortened, enhanced the maximum value of the photo-extracted current.

As foreseen by the theory, in this case the photoemission is wholly a one-photon process. This fact was confirmed by the experimental data, if the target is illuminated by low laser energies.

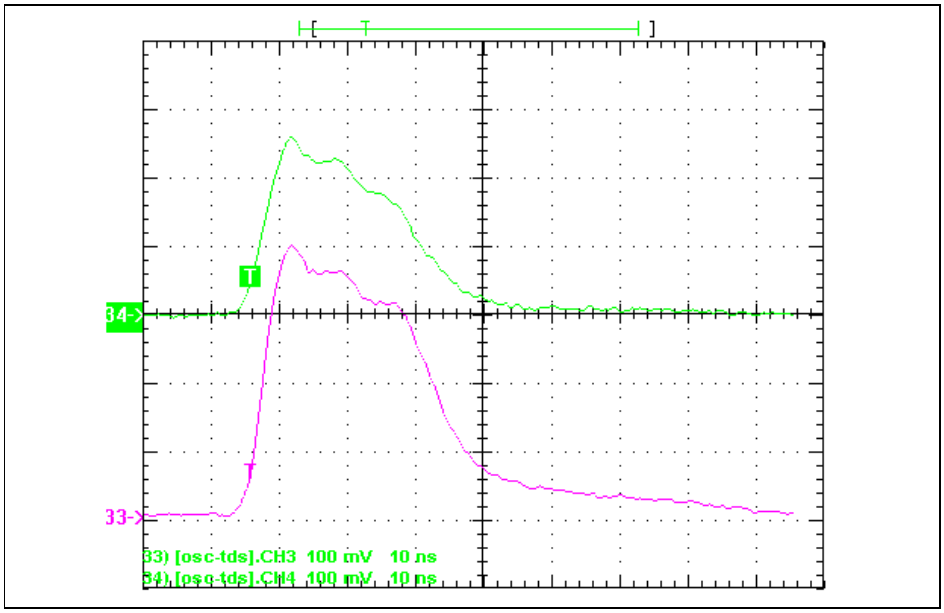

Figure 3.6 - Waveforms of laser pulse (upper trace) and current signal (lower trace), for KrF laser at 16 mJ laser energy and 10 kV applied voltage.

Figure 3.6 shows the laser and the current pulse, at 16 mJ energy and 10 kV accelerating voltage; it is very evident the similarity between the shapes of the two waveforms. In this case no plasma is produced. Increasing the accelerating voltage or the laser energy the current waveform becomes larger than the laser one.

In the figure 3.7 the normalized laser and current pulses and the temporal emission efficiency are plotted for 11 mJ incident energy and 16 kV applied voltage. The quantum efficiency was about 0.7×10^{-4} at the beginning of the laser pulse and it increased approximately of 90% close to the tail of the pulse, reaching the maximum value of about 1.3×10^{-4}. This performance is due to the plasma on the surface imperfections of the cathode, which increases lightly the charge yield close to the tail of the laser pulse (small shoulder in current pulse in fig. 3.7). By a simply one-photon process, in fact, one can expect constant emission efficiency (eq. 3.5).

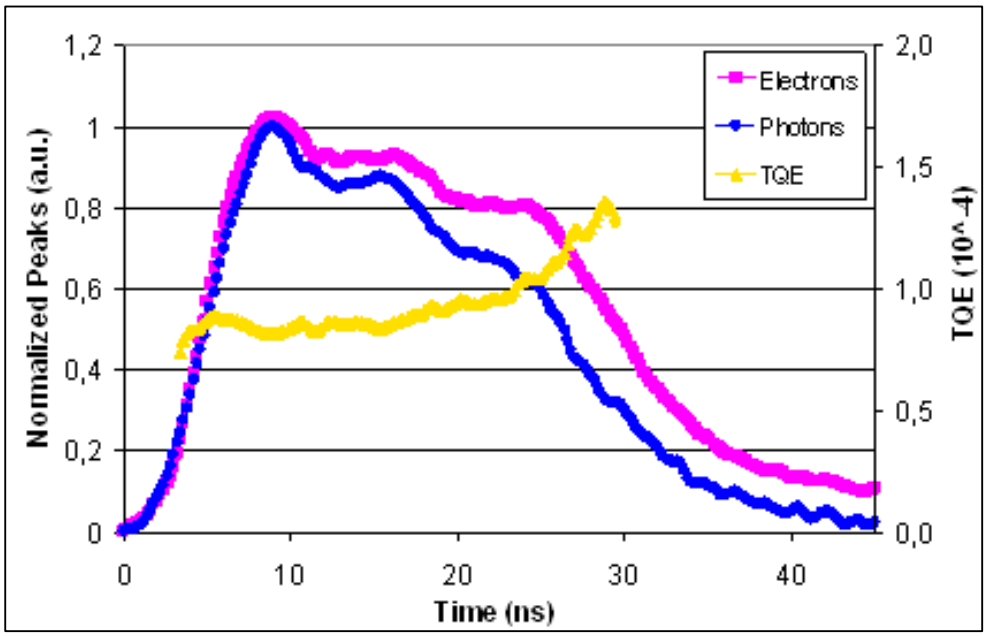

Figure 3.7 – Zn sample: normalized laser (blue line) and current (violet line) pulses, obtained by using the KrF laser at 11 mJ energy and 16 kV of applied voltage. The yellow line represents the TQE calculated in the same conditions.

3.2.3 Temperature evaluation

From equation (1.35) it is obvious that the temporal performance of the current density *J* depends on the trends of the laser intensity *I* and the temperature *T*. Therefore, in order to control the photoemitted current, the exact temporal shape of *I* and *T* is fundamental to know.

The laser waveform was simply obtained by means of the photodiode; the function *T(t)*, instead, is more difficult to estimate. This one, in fact, obeys to the following law [5]:

$$T(t) = T_o + CI_o \int_0^t g(t - t')t'^{-1/2} dt' \qquad (3.8),$$

where T_0 is the time zero temperature, $C = \frac{1 - R}{\sqrt{\pi K \rho c_s}}$, *R* is the metal reflectivity, *K* is the thermal conductivity, ρ is the mass density and c_s is the specific heat capacity; $I_0 g(t)$, besides, is the temporal profile of the laser intensity. In the present case an I_0 average value on the irradiated surface was used; the calculation of the integral was performed by means of software developed in Excel. In this way the exact temporal shape of the cathode temperature *T(t)* was obtained.

Irradiating the cathode with XeCl laser at 48 mJ energy and 50 mm^2 spot, the maximum temperature reached was about 510 K. Its temporal performance is shown in figure 3.8, together to the laser intensity waveform *I(t)*.

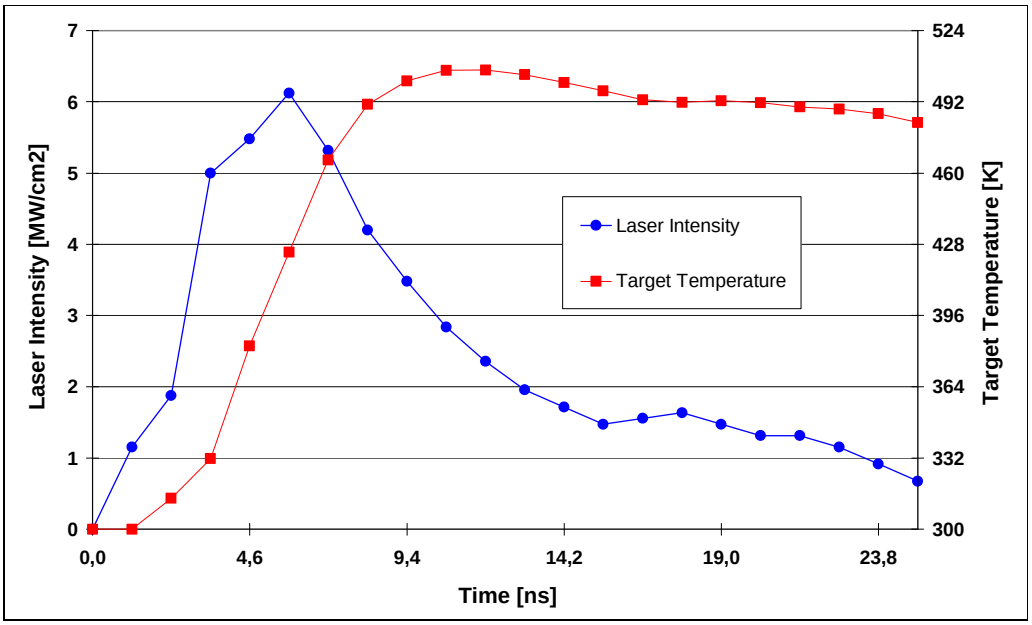

Figure 3.8 – Temperature performance of the Zn cathode irradiated by XeCl laser with 48 mJ energy and 50 mm^2 laser spot.

Besides, the temperature of the cathode irradiated by KrF laser reached the value of about 440 K, at the maximum used energy of 16 mJ and laser spot of about 40 mm^2.

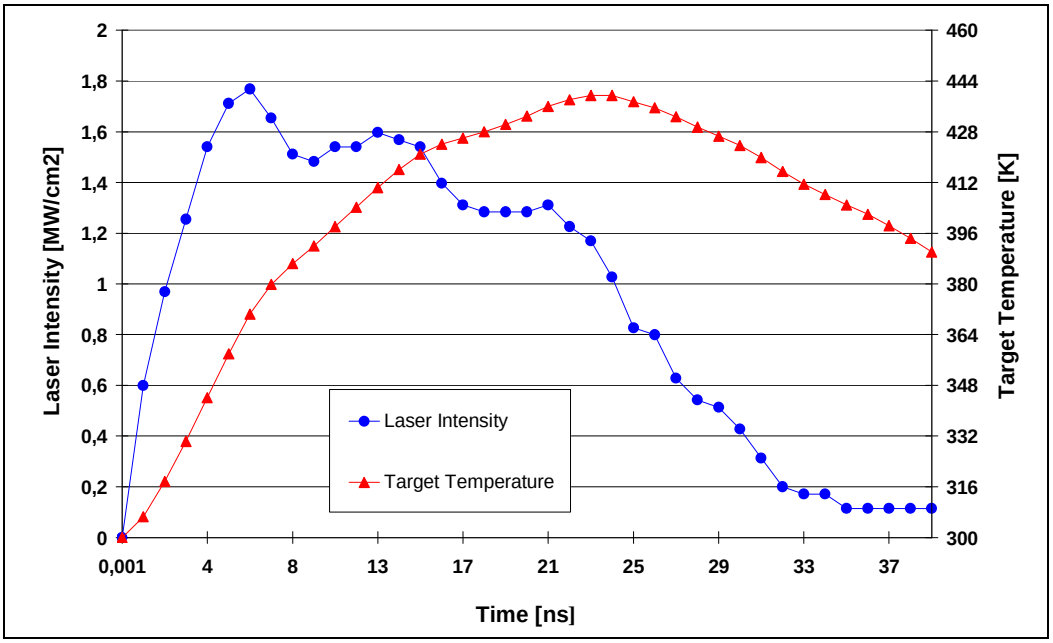

Figure 3.9 – Temperature performance of the Zn cathode, irradiated by KrF laser with 16 mJ energy and 40 mm^2 laser spot.

The obtained temperature values ruled out the thermionic emission of electrons.

From these calculations pointed out that the target temperature was, in both cases, lower than its melting point (about 700 K). The temperature so calculated refers to an ideal mirror-like surface. In the real case, the cathodes presented a “natural” surface roughness which depends on the realizing process (Fig. 3.10). The roughness involves an increase of the local temperature for Joule effect, because the higher electric field on the surface tips enhances the photoemitted current. Therefore, the combined action of the incident laser energy and the high extracted current could cause the melting of the upper layers of the tips, with a low density plasma production.

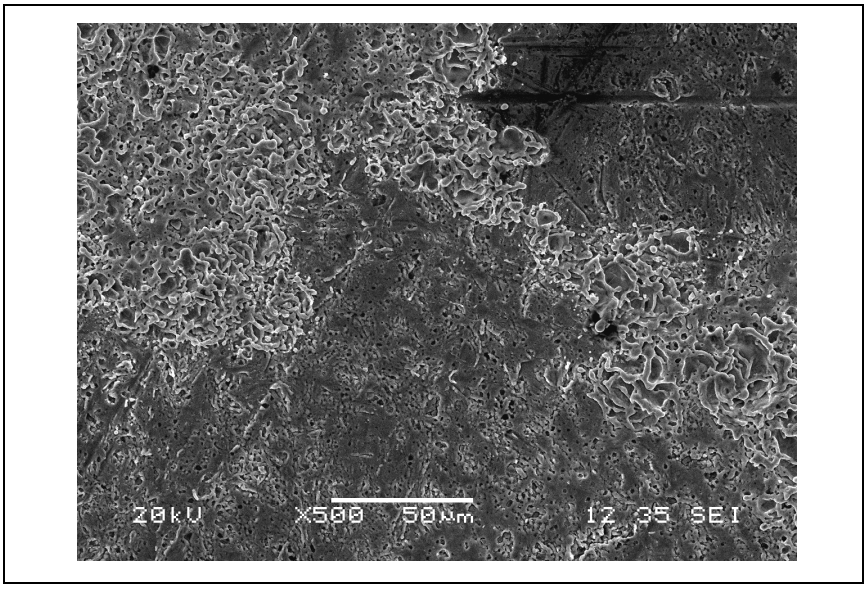

Figure 3.10 - SEM microanalysis of the Zn cathode surface before laser irradiation.

3.3 Measurements with Y cathodes

In this case the analyzed cathodes were two Y bulks with different surface morphologies. For all the Y samples the anode-cathode distance was fixed at 5 mm and the maximum applied accelerating voltage was 25 kV, limited by the presence of arcs in the gap. The cathode work function was 3.1 eV. Once more, the pulsed laser-induced photoelectric charge was measured as a function of the voltage applied between anode and cathode. In this work the measurements were performed after to have operated the vacuum into the chamber for almost two days. The experiments were performed by using XeCl, KrF and KrCl excimer lasers.

3.3.1 Results for smooth cathode

3.3.1.1 Data and analyses with XeCl laser

In this set of measures the cathode with smooth surface, placed inside the vacuum chamber, was irradiated by the XeCl excimer laser. In fig. 3.11 the peak current values vs. the accelerating voltage (0-25 kV), for 12 and 24 mJ incident laser energy, are reported. The maximum found current value was about 6.8 A, at 24 mJ and 25 kV.

The saturation effect of the current curve at 12 mJ is not present at 24 mJ, as it is possible to observe from the linear trend of the correspondent curve. This behavior is due to the plasma formation on the target surface, which is emphasized at high

incident energies or extracted current. The plasma production enhances the emitted charge over the previsions of the Fowler photoemission law (at high voltages) and the Child-Langmuir limit (at low voltages). The result is the red dot curve *I(V)*, whose is evident the linear dependence of the extracted current on the applied voltage.

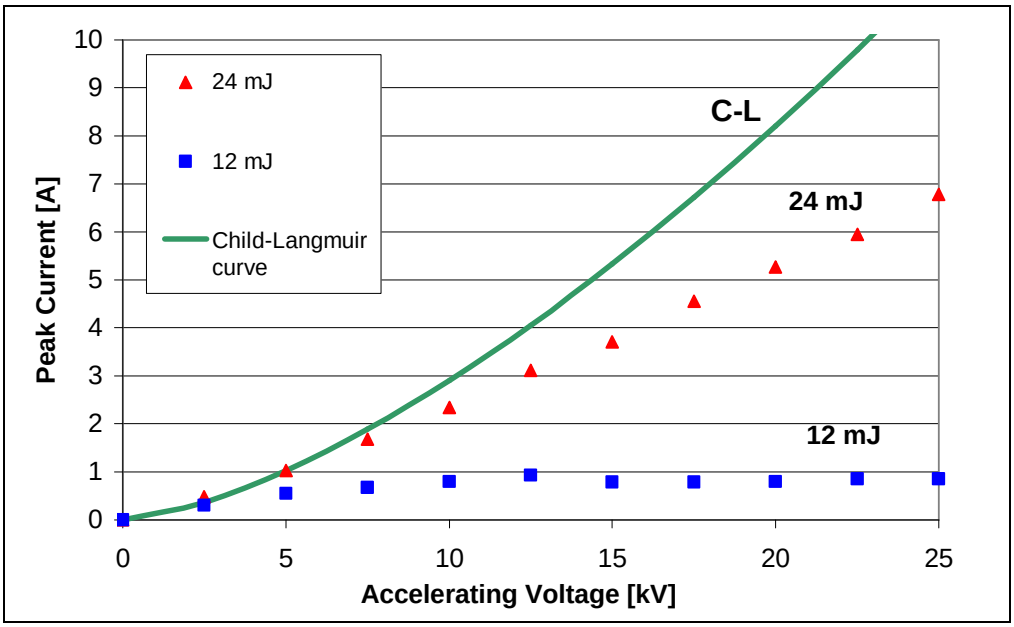

Figure 3.11 – Peak current vs. applied voltage for Y smooth sample illuminated by XeCl laser.

The quantum efficiency on time was calculated following the eq. (3.6) and plotted in fig. 3.12, under the experimental conditions of 24 mJ incident energy and 25 kV applied voltage. The TQE maximum found value was about 4.2×10^{-5}, recorded at 24 ns from the laser pulse onset time.

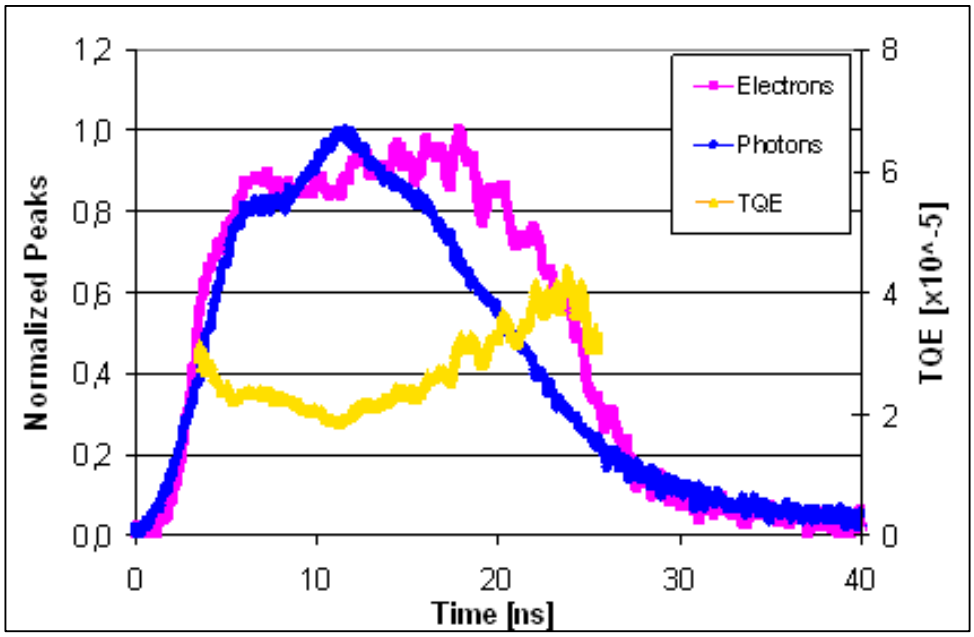

Figure 3.12 – Temporal quantum efficiency of Y smooth sample irradiated by XeCl laser. Experimental conditions: 24 mJ of laser energy and 25 kV of applied voltage.

By using the eq. (3.8), it pointed out that the maximum temperature reached by the Y smooth target during the experiment was close to 800 K (at 24 mJ incident laser energy and 50 mm^2 of laser spot), close to 16 ns from the beginning of the laser pulse (fig. 3.13). Although also this value is lower than the melting point of the material, the production of a low plasma density and the Schottky effect, due to the local imperfections however present on the surface (fig. 3.14), enhance the photo-extracted current and the emission efficiency (fig. 3.12).

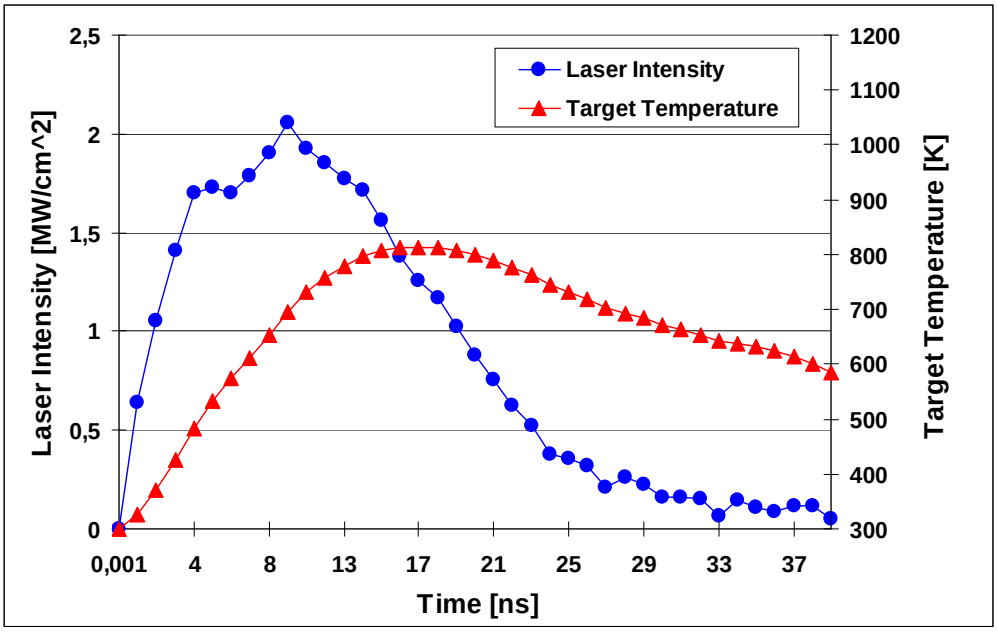

Figure 3.13 – Temperature behavior of the Y smooth target irradiating by XeCl laser with 24 mJ energy and 50 mm^2 laser spot.

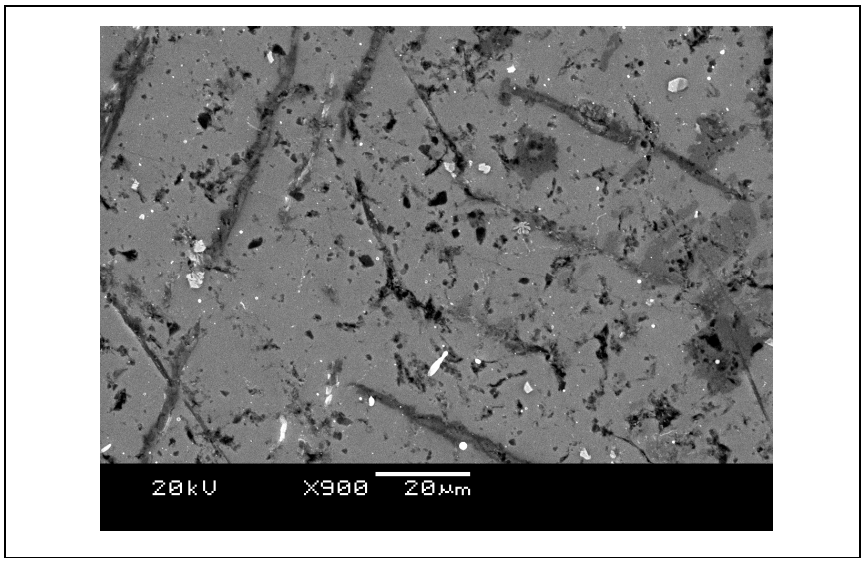

Figure 3.14 – SEM microanalysis of the Y smooth sample surface before laser irradiation.

3.3.1.2 Data and analyses with KrF laser

Fig. 3.15 shows the experimental results for the same cathode illuminated by KrF laser: peak current as a function of the accelerating voltage, evaluated at the same laser energies used in the previous measurements. Even in this case, the sample was illuminated by several laser shots (with the same spot/fluence), in order to ablate pollution and possible oxides from the target surface.

The maximum output current was 9.3 A, reached at 24 mJ laser energy and 25 kV applied voltage. For 16 and 12 mJ the current peak was about 3.8 A and 2.4 A, respectively. Once more, the current peak curves have a positive slope that increases with the laser energy and the data overcome the Child-Langmuir limit at low voltages. Again, these behaviors are explained with the influence on the photocurrent of plasma formation and Schottky effect.

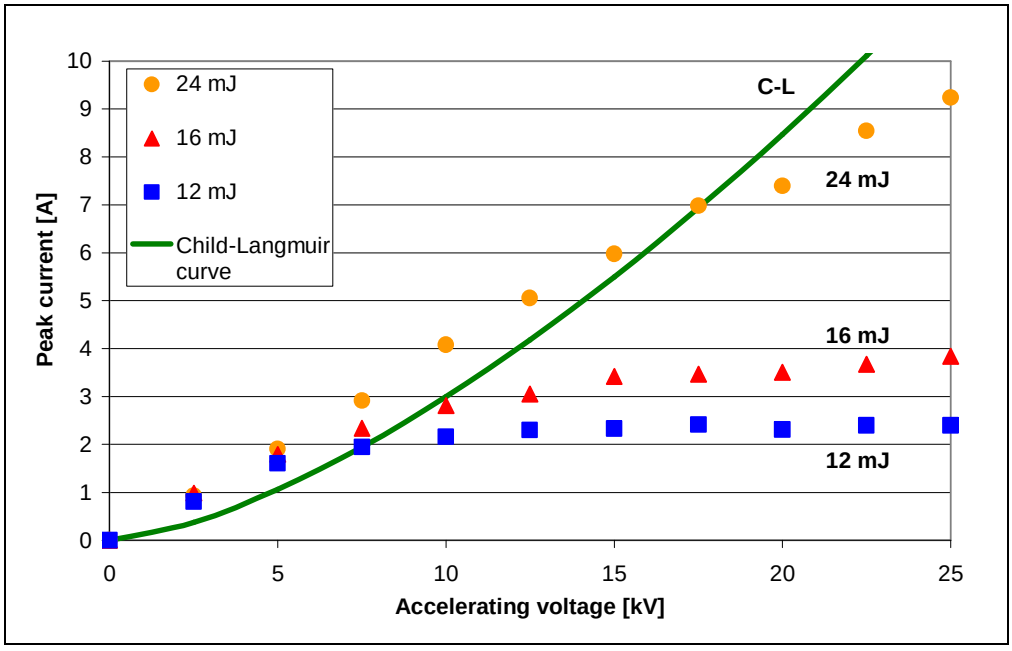

Figure 3.15 – Peak current vs. applied voltage for Y smooth sample illuminated by KrF laser.

The quantum efficiency was calculated as a function of the time, following the same calculation procedure (fig. 3.16). Its maximum value, registered at 33 ns, was approximately 6.0×10^{-5}, obtained at 24 mJ incident energy and 25 kV applied voltage. This efficiency value is higher than the one carried out irradiating the same target with XeCl laser in the similar experimental conditions (3.8×10^{-5}).

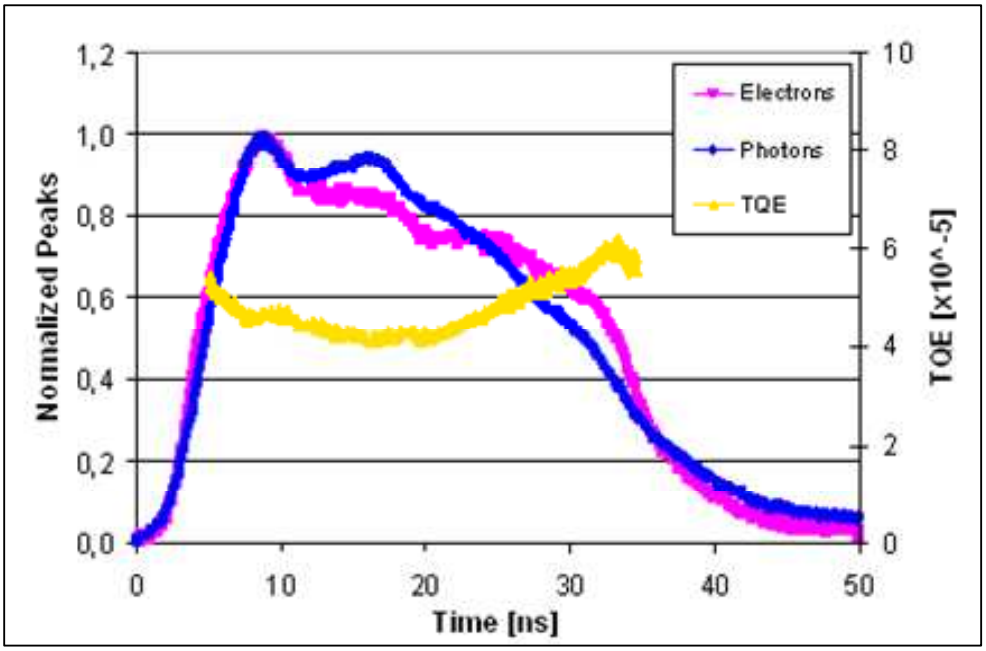

Figure 3.16 – Smooth Y sample: Normalized laser (blue line) and current (violet line) pulses, obtained by using the KrF laser at 24 mJ energy and 25 kV of applied voltage. The yellow line represents the TQE calculated in the same conditions.

The relatively low current and efficiency values suggested to irradiate by laser the sample with high incident energy, in order to remove impurities and oxide layers. Practically, the operation was performed by putting away the neutral filters placed at the laser gate and keeping a 10 kV accelerating voltage between anode and cathode. The incident laser energy was about 100 mJ. Strong discharges in the anode-cathode gap were observed in consequence of this treatment. The combined action of incident

laser energy and the high current crossing the target surface induces the melting of the surface layer, creating a new rougher surface, full of micro-tips and valleys (fig. 3.17).

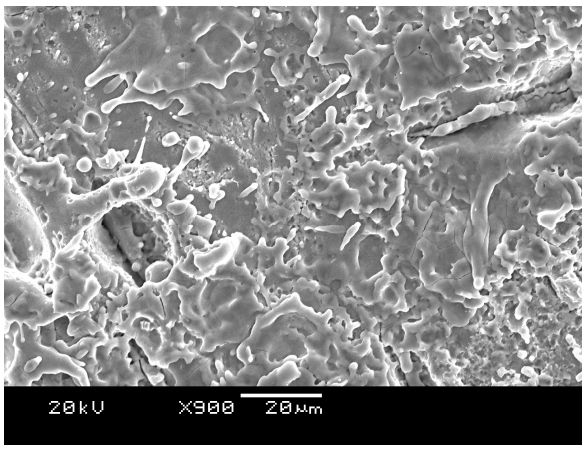

Figure 3.17 – SEM microanalysis of the Y smooth surface, after discharges induced by high incident energy.

Irradiating the target at 12 mJ laser energy and plotting the photo-current vs. voltage, it was possible to note that, in this case, the extracted charge is higher than the one obtained before at the same incident energy (figure 3.18). The maximum laser energy used was limited by the occurrence of electric arcs. In this case the maximum output current was about 8.5 A, reached at 25 kV of accelerating voltage, in opposition to the value of about 2.5 A obtained in the first measure set. It was clear that the cause of this behavior is due to electric breakdowns induced on the cathode which increased its superficial roughness.

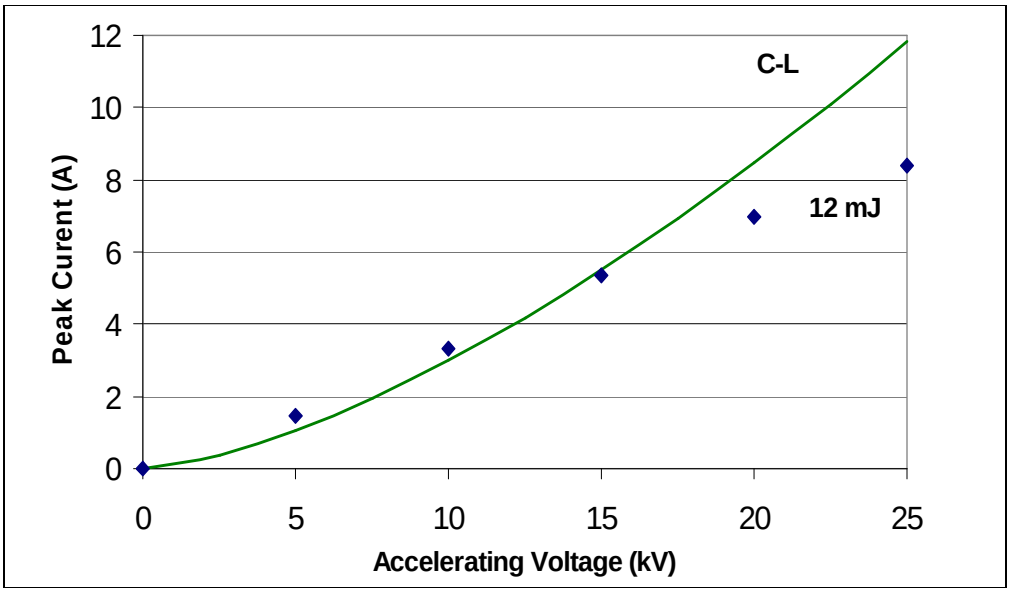

Figure 3.18 – Peak current vs. voltage at 12 mJ energy for Y smooth sample, after inducing breakdowns.

It has been very interesting to calculate the extraction efficiency in these operating conditions. The values found are plotted in fig. 3.19: the maximum value of TQE was about 3.3×10^{-4}, recorded close to 33 ns from the laser pulse onset time.

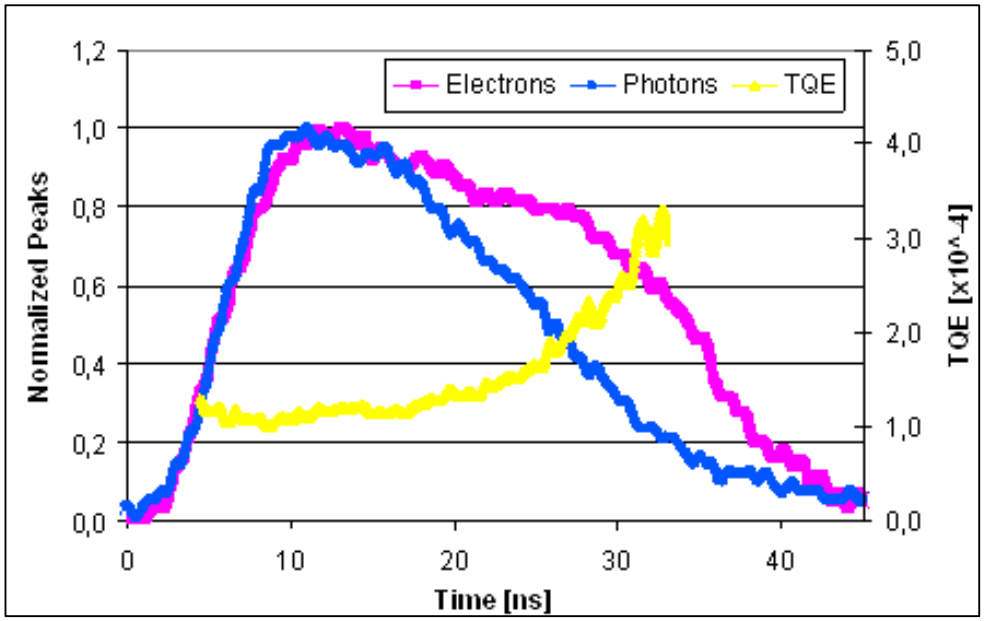

Figure 3.19 – Temporal quantum efficiency for smooth Y sample irradiated by KrF laser, after inducing discharges. Experimental conditions: 12 mJ of laser energy and 25 kV of applied voltage.

It is evident the growth of the efficiency close to the shoulder of the current curve, at the tail of the laser pulse. This increase of the photoemitted current is, once again, due to the plasma formation on the more irregular surface.

3.3.2 Results for rough cathode

3.3.2.1 Data and analyses with KrF laser

In the Figure 3.20 the experimental results for rough cathode are reported: peak of photo-extracted current as a function of the voltage applied in the gap. The measures were executed at three different laser energies: 12, 16 and 24 mJ.

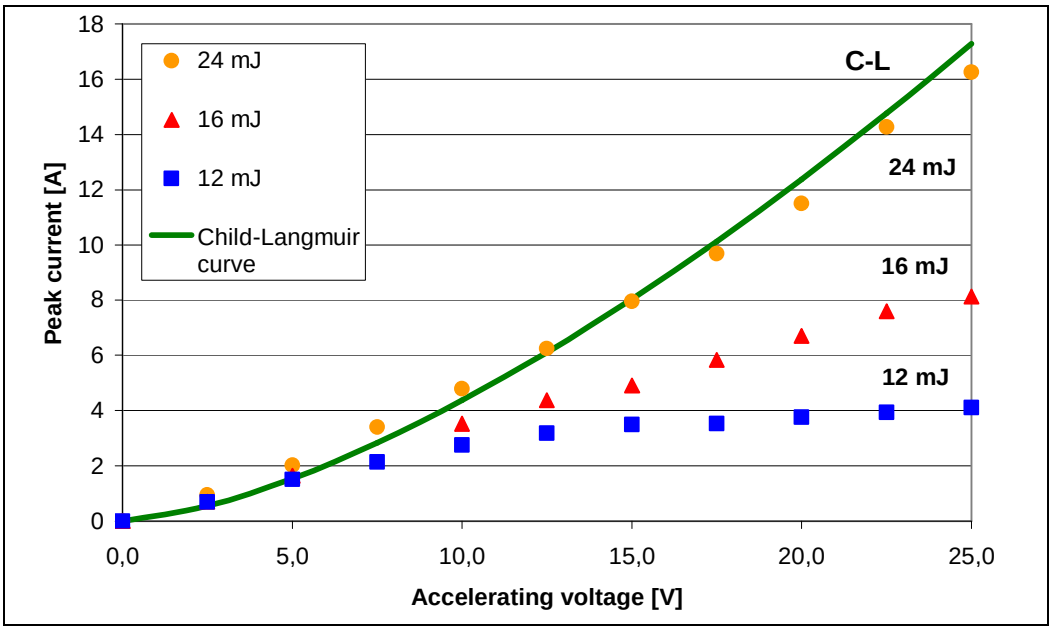

Figure 3.20 – Peak photocurrent vs. applied voltage for Y rough sample irradiated by KrF laser, at three different energies.

The maximum output current achieved was about 16.3 A, at the incident laser energy of 24 mJ. For 16 and 12 mJ the maximum current was about 8 and 4 A, respectively. The current curves present, also in this case, a positive slope that increases with the laser energy and the data overcome the Child-Langmuir limit at low voltages. As seen above, even in this case these behaviors could be explained by the influence on the photocurrent of plasma formation and Schottky effect.

The temporal quantum efficiency was calculated by the formula (3.6), in these experimental conditions: 24 mJ laser energy and 25 kV applied voltage. Its maximum value was recorded at 33 ns from laser onset time and was about 1.2×10^{-4} (fig. 3.21).

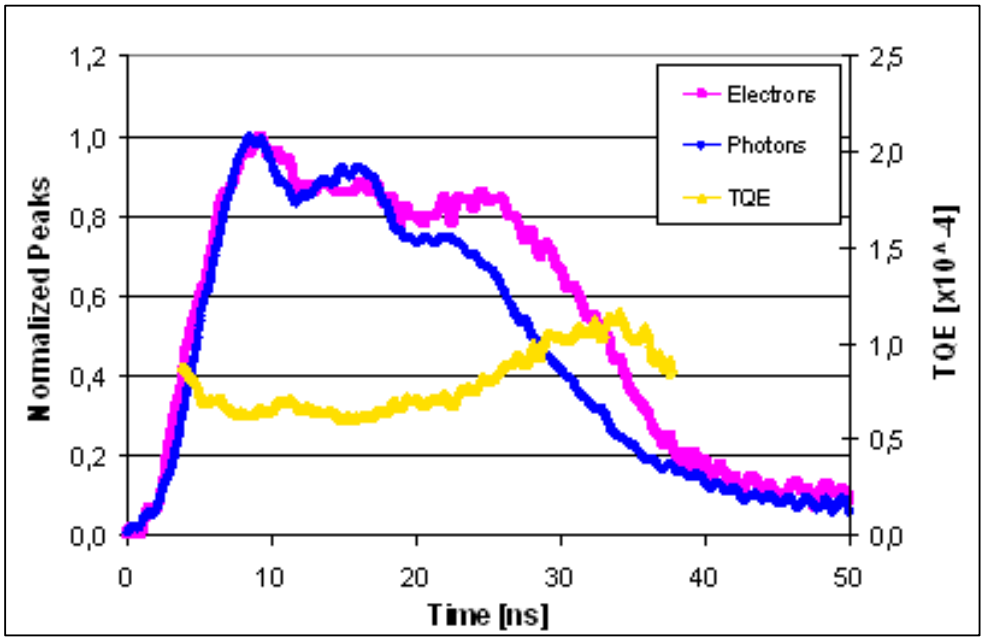

Figure 3.21 – Rough Y sample: Normalized laser (blue line) and current (violet line) pulses, obtained by using the KrF laser at 24 mJ energy and 25 kV applied voltage. The yellow line represents the TQE calculated in the same conditions.

During the electron extraction the sample roughness decreases, due to the melting of the superficial tips. Therefore, after this set of measures, we tried to enhance the

roughness of the surface. For this purpose the target was illuminated by high energy laser beam (approximately 100 mJ). Again, this operation was performed by removing the neutral filters, placed close to the laser window. This action induced electric breakdowns in the anode-cathode gap, whose consequence was the increasing of the surface irregularity of the target. Local imperfections were generated, whose dimensions and periodicity were smaller than the one pre-existent, due to the treatments by the machines. In figure 3.22 it is possible to observe SEM images of the cathode surface before and after the high energy irradiation to enhance its roughness.

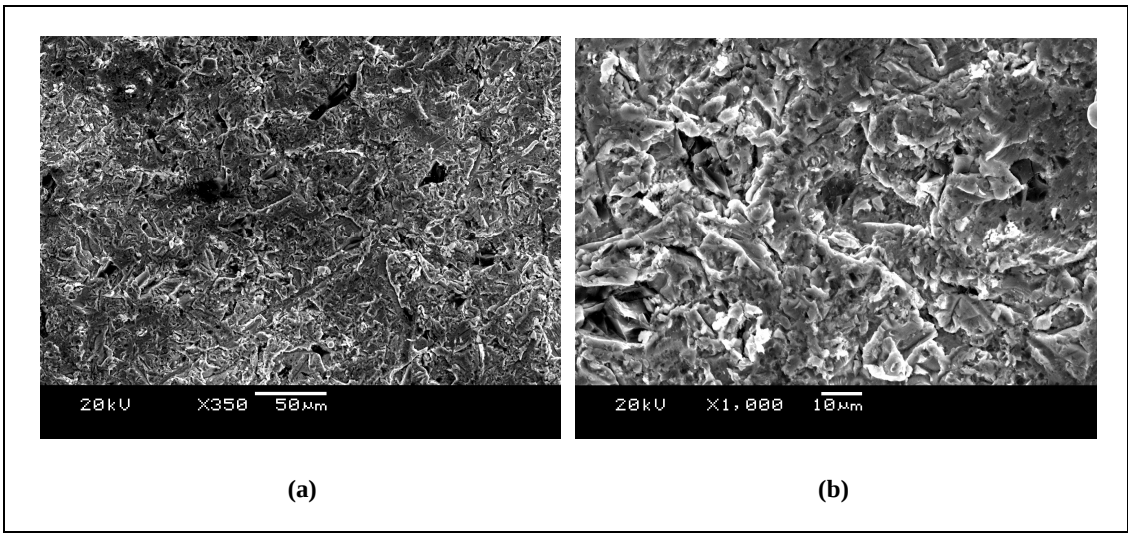

Figure 3.22 – SEM microanalyses of the Y rough sample surface, before (a) and after inducing discharges (b).

Measuring, after this phase, the current vs. voltage at 12 mJ energy, it was possible to observe that the extracted charge is higher than the one obtained before at the same incident energy (figure 3.23). The laser energy used was limited by the occurring of electric arcs.

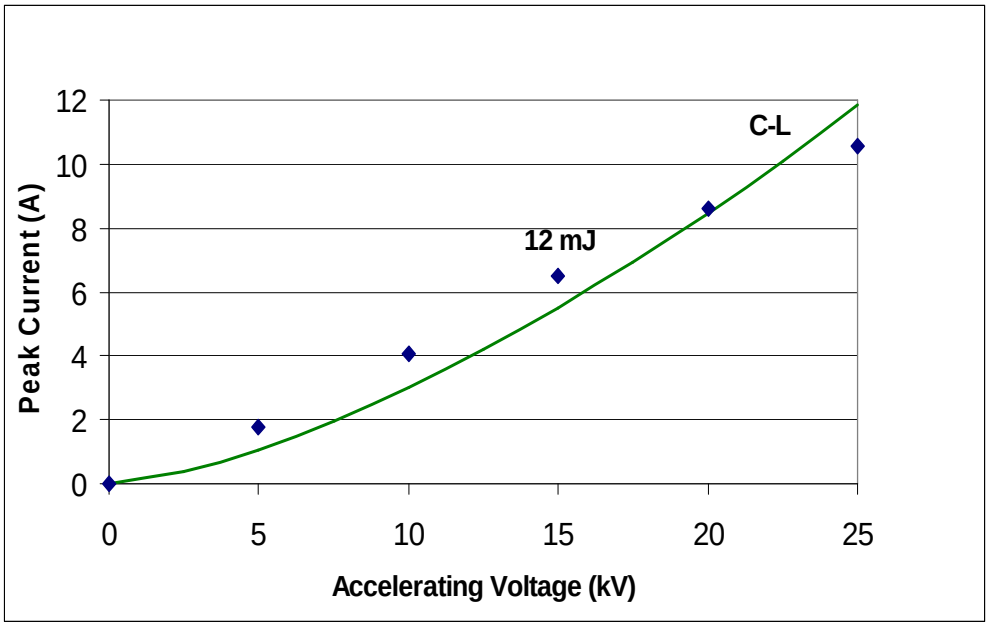

Figure 3.23 – Peak current vs. voltage at 12 mJ energy for Y rough sample irradiated by KrF, after inducing breakdowns.

In this case the maximum output current was about 10.5 A, reached at 25 kV of accelerating voltage, in opposition to the value of about 4 A obtained in the first measure set. It was clear that the cause of this behavior is that electric discharges induced on the cathode had increased even more its surface roughness. As a consequence, also the temporal quantum efficiency enhanced, if measured after the induced electric breakdowns. In fig. 3.24 is plotted the calculated TQE for 12 mJ incident laser energy and 25 kV of applied voltage: its maximum value found in these conditions was about 6.7×10^{-4}, reached after about 32 ns from the laser onset time. This value of emission efficiency was the highest found in this experimental work and was due at the higher concentration of plasma product on the rougher surface. This interpretation was confirmed by the large shoulder at the tail of the photocurrent waveform (fig. 3.24).

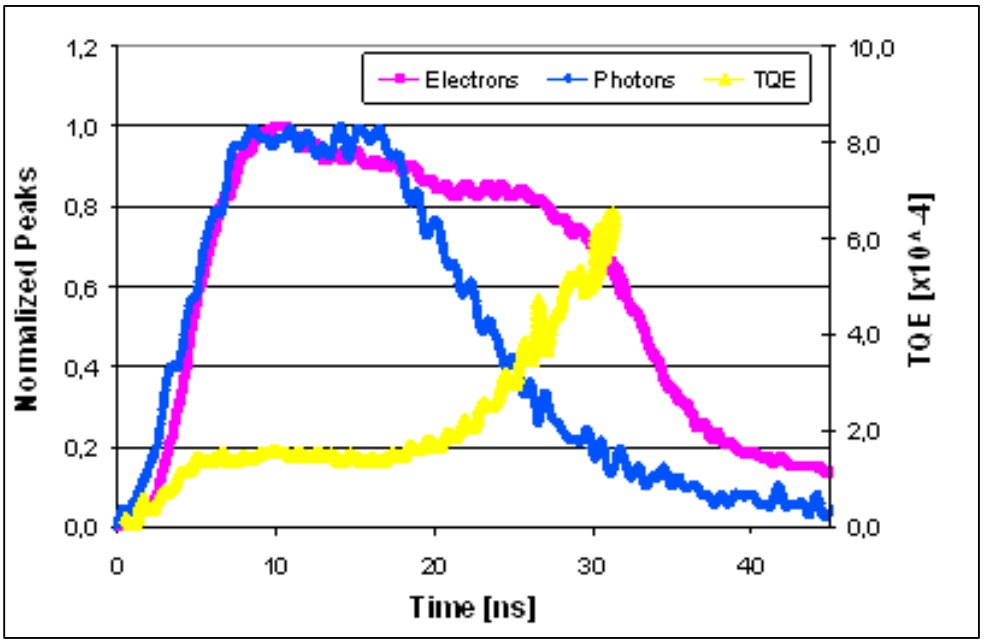

Figure 3.24 – Temporal quantum efficiency of Y rough sample irradiated by KrF laser, after inducing discharges. Experimental conditions: 12 mJ of laser energy and 25 kV of applied voltage.

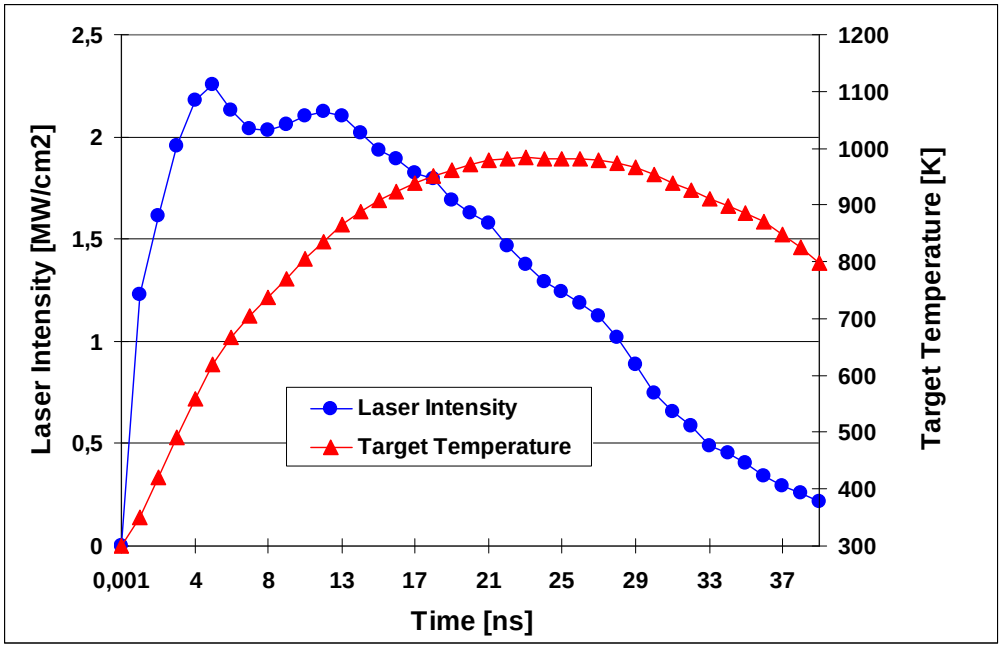

Figure 3.25 – Performance of the temperature of the Y cathode, irradiated by KrF laser with 24 mJ energy and 40 mm^2 laser spot.

Calculating the average temperature of the sample surface at 24 mJ of incident energy and 40 mm^2 of laser spot, a maximum value of about 980 K was found. This last was recorded at 23 ns from the beginning of the laser action (fig. 3.25). This temperature refers to an ideal mirror-like surface, while on the local imperfections of the cathode surface the melting point is probably reached.

3.3.2.2 Data and analyses with KrCl laser

In another experimental stage the Y rough target was illuminated by KrCl excimer laser, as to analyze the changes on electron emission due to the photon energy. Two different laser energies were used: 12 and 20 mJ. The measurements were performed only in one day, because of the fast degrading of the mixture that generates the laser action.

The extracted currents are shown in fig. 3.26 as a function of applied voltage. The maximum current value was about 21.5 A, found at 20 mJ of incident laser energy and 25 kV of accelerating voltage. This current was higher than the one extracted by the same sample by using KrF laser under similar experimental conditions (16.3 A obtained at 24 mJ of incident energy and 25 kV of applied voltage).

Even for 12 mJ the photocurrent was higher than the one obtained in the case of Y rough target irradiated by KrF source under the same experimental conditions (approximately 15 A at 25 kV for the KrCl laser, in opposition to 4 at 25 kV for the

KrF laser). It is clear that this behavior was due to the higher photon energy of KrCl (5.6 eV) with respect to the KrF one (5 eV).

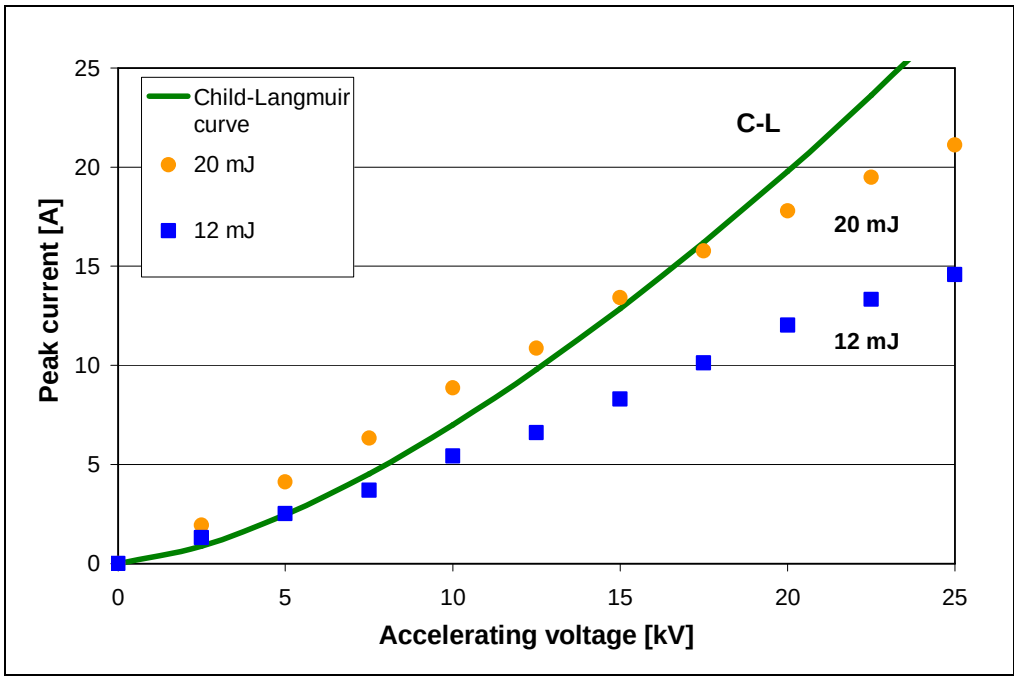

Figure 3.26 – Peak current vs. accelerating voltage for Y rough sample irradiated by KrCl laser.

The little shoulder in the current waveform, present at the tail of the laser pulse (fig. 3.27), was index of plasma production on the rough surface. The quantum efficiency reached, in fact, a maximum value of 1.5×10^{-4}, localized in the neighborhood of 12 ns.

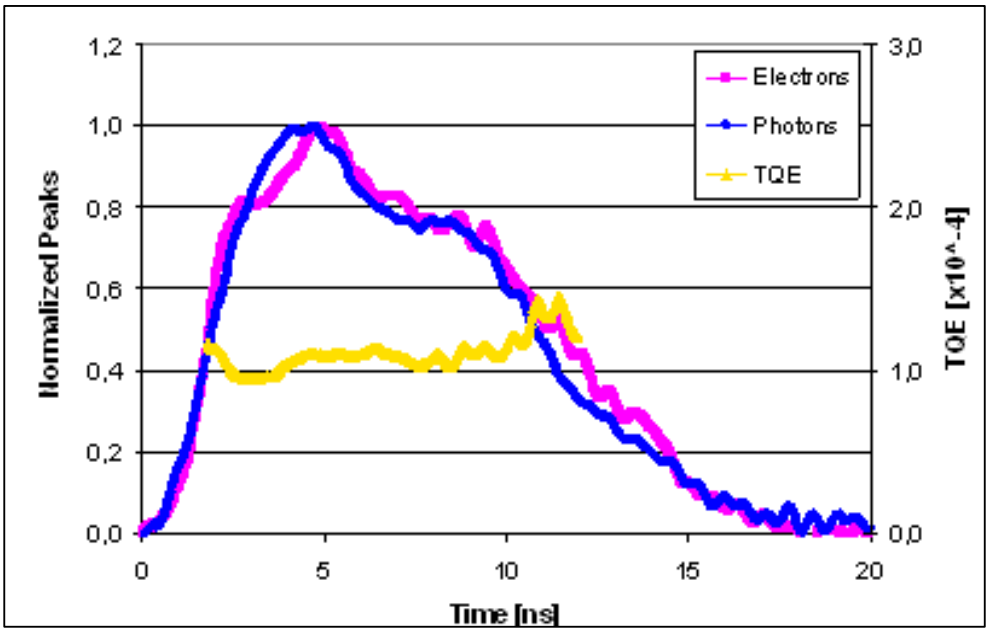

Figure 3.27 – Temporal quantum efficiency of Y rough sample irradiated by KrCl laser. Experimental conditions: 20 mJ of laser energy and 25 kV of applied voltage.

Temperature calculations, in fact, confirmed this interpretation: the maximum surface temperature was about 700 K (reached at 9 ns from the laser pulse onset time), lower than the KrF one (fig. 3.28).

Even in this case, we tried of enhance the electron emission by creating micro-irregularities on the target surface. The same procedure of the electric breakdowns stimulated by increasing the incident energy was performed. Irradiating, in these conditions, the target at 12 mJ laser energy, the extracted charge was higher than one found previous to the surface modification: 19 A in opposition to 14.5 A (fig. 3.29).

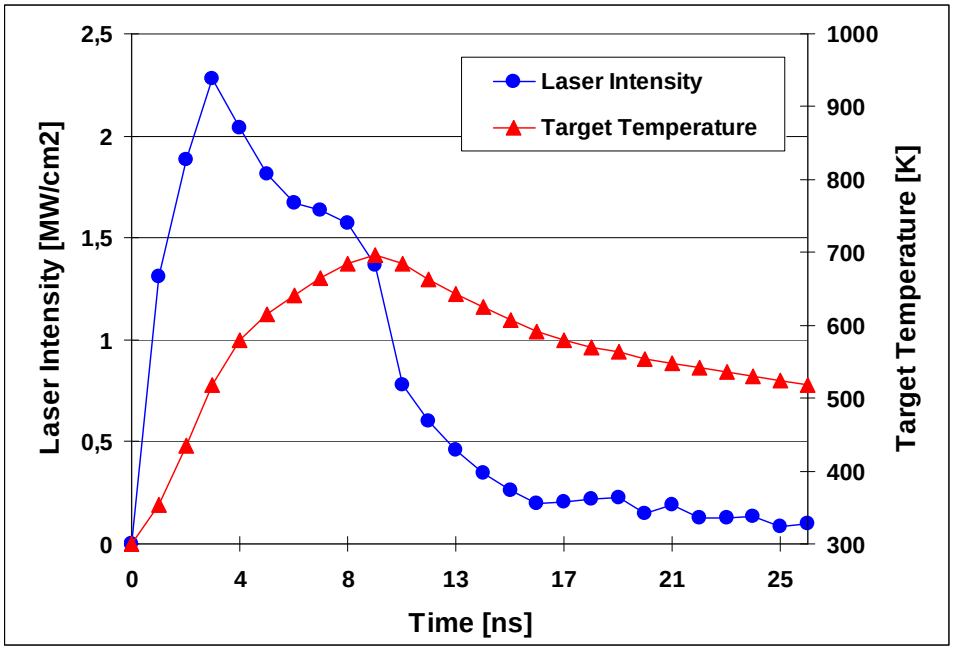

Figure 3.28 - Temperature evaluation of the Y cathode surface irradiated by KrCl laser with 20 mJ energy and 70 mm^2 laser spot.

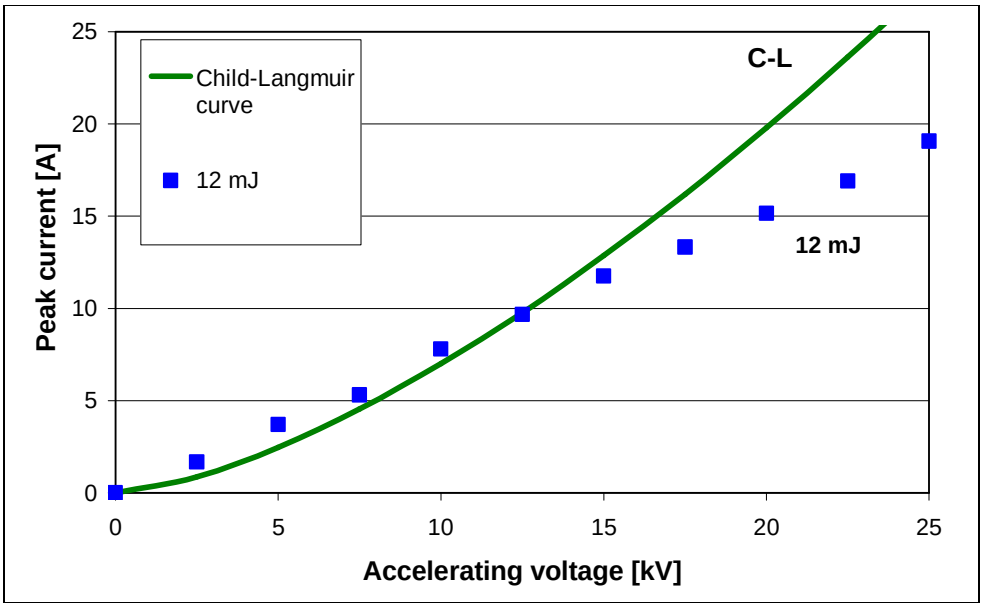

Fig. 3.29 – Peak current vs. accelerating voltage for Y rough cathode irradiated by KrCl laser at 12 mJ energy, after inducing breakdowns.

In this case the quantum efficiency increased from 1.5×10^{-4} to 4.0×10^{-4} (fig. 3.30), more than the double of the prior found value.

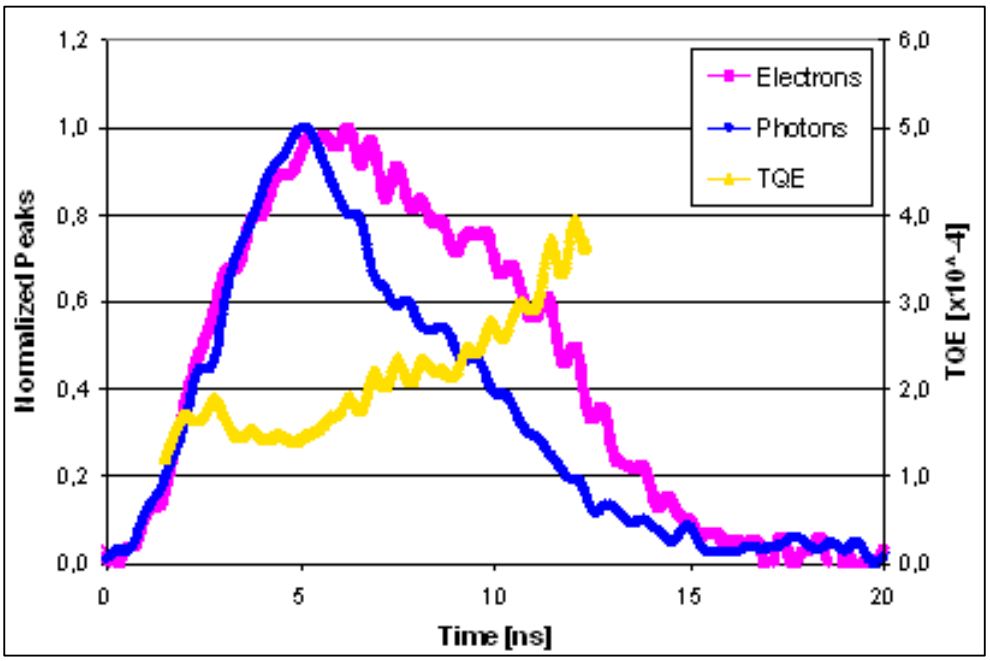

Figure 3.30 – Temporal quantum efficiency of Y rough sample irradiated by KrCl laser, after inducing breakdowns. Experimental conditions: 12 mJ of laser energy and 25 kV of applied voltage.

3.3.3 Time behavior

In another experimental phase, the performance of the photo-emitted current on time was studied. Two different repetition rates of incident laser energy on target were used, in order to analyze the photo-emission behavior for low and high total extracted charge: fixed the same observation time, in fact, different repetition rate means different number of incident laser pulses.

The cathodes examined were smooth and rough Y, the energy source was the KrF laser at 12 mJ, the accelerating voltage fixed at 10 kV, while the repetition rates used were 1 and 10^{-3} Hz.

Preliminary operation was the electric breakdowns induction by means of high incident laser energy on each target. The purpose was to enhance the surface roughness, as to obtain a high current starting value. For both cathodes the photo-extracted current was monitored and recorded for 10000 s, at 1 Hz of laser action. The same procedure was repeated for the second rate of incident laser energy (10^{-3} Hz). Electric discharges were performed between the two steps, in order to restore the initial value of extracted charge, because of the reestablishment of the original superficial irregularity.

Figs. 3.31 and 3.32 show the comparison between the temporal behavior of rough and smooth cathode. They point out that after about 10000 s the photocurrent at 1 Hz lessened about 50% and 40% for the rough and smooth cathode, respectively, while it is different for the temporal trend at 10^{-3} Hz. After 10000 s it decreased of about 18% and 6 % for the rough and smooth cathode, respectively.

Indeed, inducing electric breakdowns, by increasing the laser energy incident on the cathodes, the initial values of current peak and QE were restored. This behavior can be explained if one considers that each laser shot reduces the roughness of the target surface, due to the melting of the tips. This process reduces the local electric field and, as a consequence, the output current.

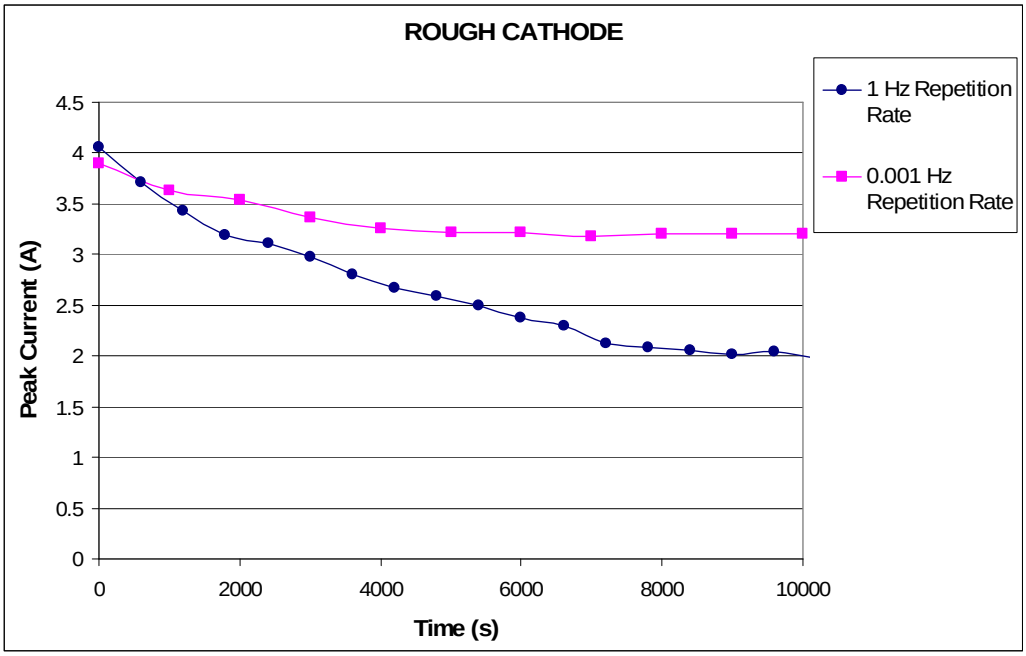

Figure 3.31 – Time performance of the photocurrent for Y rough sample irradiated by KrF laser at 1 Hz (blue line) and 10^{-3} Hz (violet line). The incident laser energy was 12 mJ, while the applied voltage was 10 kV.

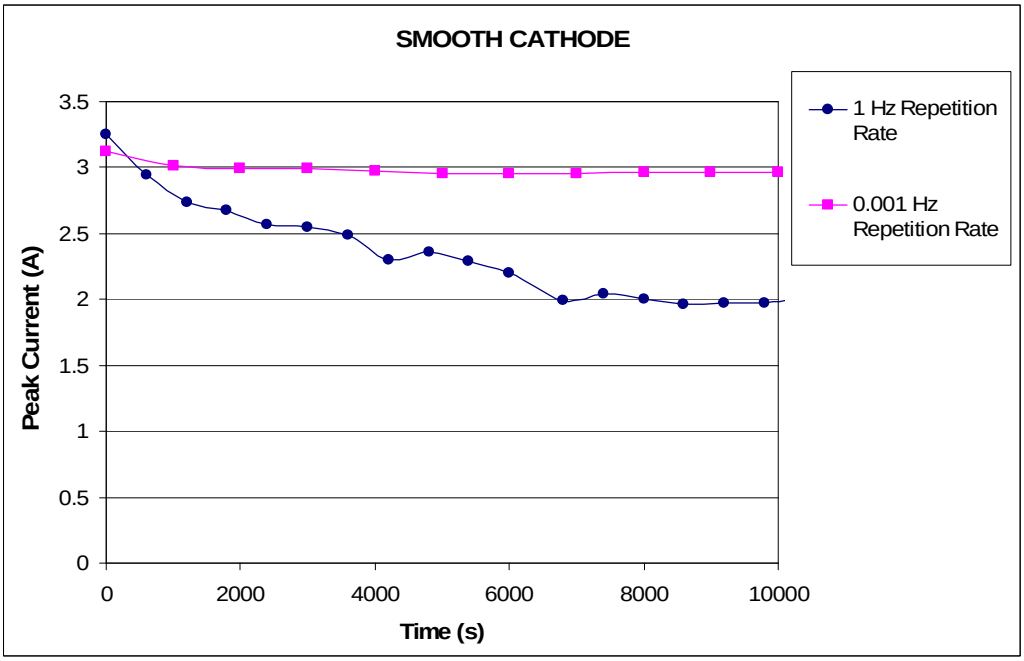

Figure 3.32 – Time performance of the photocurrent for Y smooth sample irradiated by KrF laser at 1 Hz (blue line) and 10^{-3} Hz (violet line). The incident laser energy was 12 mJ, while the applied voltage was 10 kV.

At 10^{-3} Hz the photoemission didn't decrease on time like for the 1 Hz laser irradiation, confirming that for little extracted charge the surface morphology didn't change substantially. The above results were also confirmed by SEM microanalyses of cathode surfaces which showed melted irregularities on the rough and smooth target after 10000 s at 1 Hz repetition rate (figures 3.33c and 3.33d).

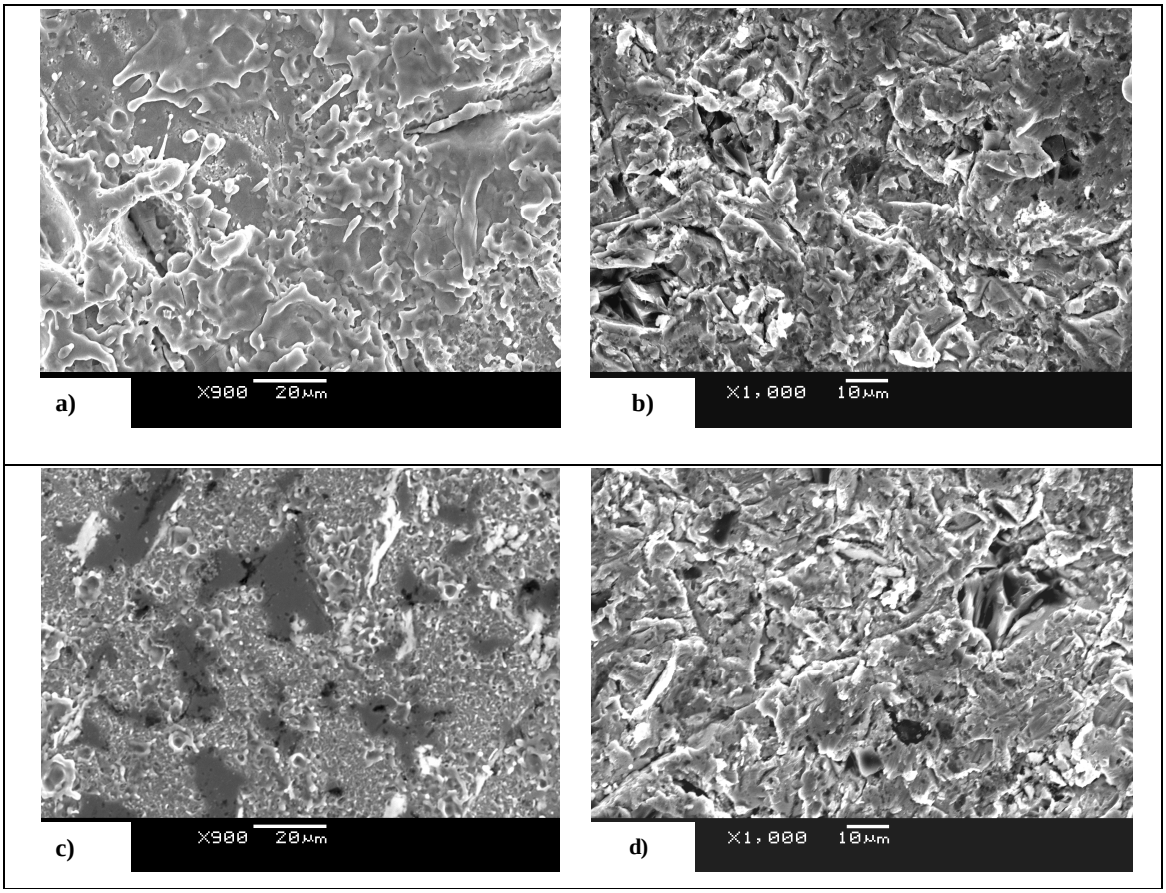

Figures 3.33 - SEM images of the Y cathode surfaces, irradiated by KrF laser at 1Hz repetition rate:
a) smooth sample after electric discharges; b) rough sample after electric discharges;
c) smooth sample after 10000 incident laser pulses; d) rough sample after 10000 incident laser pulses.

3.4 Emittance evaluation

Emittance calculations for each metal target and laser energy source were performed in this work. An evaluation of the angular dispersion for all the produced electron beams was given by using the formula (1.47):

$$\varepsilon_{N\,rms} = \gamma \frac{r}{2} \sqrt{\frac{nh\nu - \phi}{mc^2}} \qquad (3.9).$$

The plot in fig. 3.34 shows the normalized emittance calculated by means of the above equation for Y and Zn samples, under different wavelength laser irradiation. The best-value for the beam normalized emittance ε_N is about 1.2 π mm mrad, reached at 248 nm (KrF laser) with Zn cathode. For Y target the lowest emittance value, 1.5 π mm mrad, is obtained by irradiating it with XeCl laser: this behavior is due to the small difference between XeCl photon energy and Y work function. The relatively high emittance value, calculated for Zn sample illuminated by XeCl laser, is due to the dominance of the two-photon effect, because the XeCl photon energy (4.02 eV) is lower than the Zn theoretical work function (4.33 eV).

From this considerations, carried out that another advantage in using metal cathodes is the possibility to control easily the angular spread of the extracted beam, only by choosing opportunely the incident energy source (λ) and the target material (ϕ).

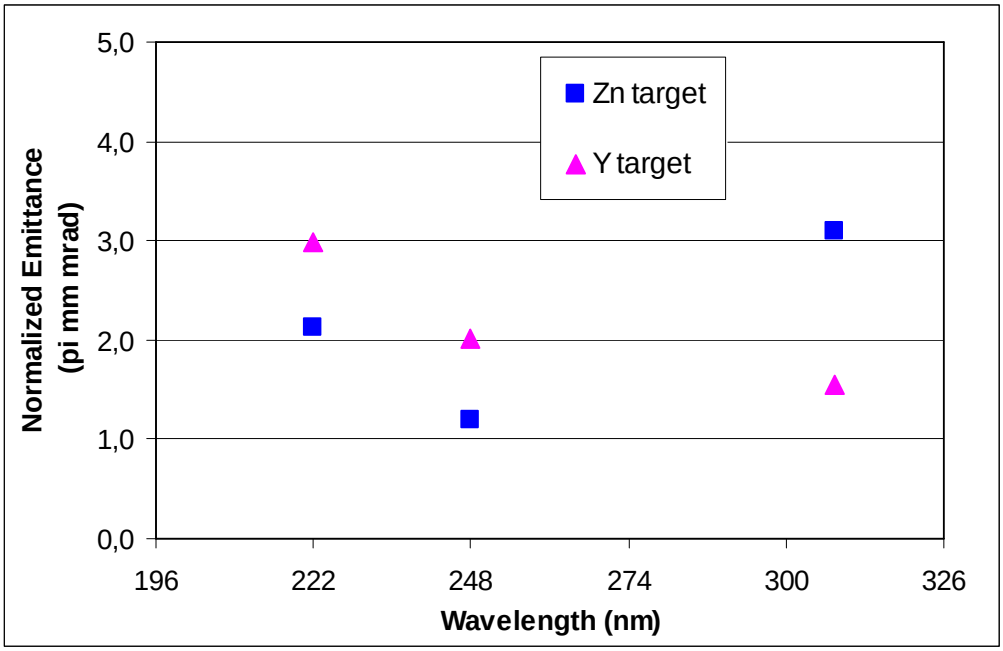

Figure 3.34 – Normalized emittance calculated by using eq. (3.9), for Y and Zn samples irradiated by excimer lasers.

The surface roughness of the cathode modifies the emittance values, because of the decreasing of the metal work function due to the Schottky effect and the plasma formation on the tips. The combination of these two effects involves an increase of the angular divergence for the produced electron beams.

References Chapter 3

[1] V.V Choulkov, *"Effect of natural roughness on electron emission from metal in electric field"*, IEEE CP **1**, 17 (2004).

[2] M.S. Causo, M. Martino and V. Nassisi, Appl. Phy. **B 59**, 19 (1994).

[3] L. Martina, V. Nassisi, G. Raganato and A. Pedone, Nucl. Instrum. Meth. **B 188**, 272 (2002).

[4] D. Doria, A. Lorusso, F. Belloni, V. Nassisi, L. Torrisi and S. Gammino, Laser Part. Beams, **22**, 461 (2004).

[5] J. Lin and T.F. George, "*Laser-generated electron emission from surfaces: Effect of the pulse shape on temperature and transient phenomena*", J. Appl. Phys. **54**, 382 (1983).

4 Theoretical model and simulation

4.1 Introduction

In this chapter a theoretical model was developed in order to obtain the electric field values on the rough surface of the cathode and to calculate the surface rate with higher electron emission. Besides, the results of simulations performed by OPERA 3-D program are reported, in order to obtain electron-beam trajectories and a photo-current estimation close to the whiskers of the irregular surface.

The results obtained were compared with the ones experimentally observed, in order to understand if, by modifying in another way the surface characteristics of the target, it is possible to improve the extracted ion-beam quality.

4.2 Theoretical model

The surface roughness can be simply modelled by choosing a trial electric potential. For sake of simplicity, the potential is *y*-independent, so it is limiting itself to

consider ripples only in the *x*-direction. Putting the perpendicular direction to the surface along the *z* axis, the electric potential *V* is:

$$V(x,z) = \theta \exp\left(-\frac{2\pi}{a} z\right) \cos\left(\frac{2\pi}{a} x\right) + \eta \frac{z}{a} + \kappa \qquad (4.1),$$

where η and κ are constants that depend on the boundary conditions, namely the cathode and anode voltages, *a* is a parameter that describes the tips periodicity onto the target rough surface and θ controls their height. In the present case *a* can be chosen in the range 1-10 μm, because of the real periodicity of the irregularities on the cathode surface, pointed out from profilometer and SEM analyses. This potential satisfies the Poisson equation.

Matching the expression (4.1) to a constant, namely $V = 0$, it was found the equation for the equipotential metallic surface. Such an equation can be analytically solved, and the solution given in terms of Lambert's product-log function [1]. This function is the solution of Lambert's equation and it is the inverse function of $x = W \cdot e^{W}$. It is not very simple to write the analytical expression of this function, but it is possible to point out its Taylor's series around zero value:

$$W(x) = \sum_{n=1}^{\infty} \frac{(-n)^{n-1}}{n!} x^{n} \qquad (4.2).$$

As a consequence, it has preferred just to draw, by using MATHEMATICA software, the surface profile choosing the following parameters (fig. 4.1):

$$\theta \rightarrow 1 \text{ V}, \; a \rightarrow 10^{-6} \text{ m}, \; \eta \rightarrow 10 \text{ V}, \; \kappa \rightarrow -1 \text{ V}$$

For such choice of parameters, the amplitudes of the undulations of metallic surface are of the order 0.1 μm, which is compatible with the observations of the superficial imperfections created after inducted electric breakdowns. Considering only this set of parameters, MATHEMATICA represents the potential and the strength of the electric field with the chromatic scales, like in the fig. 4.2.

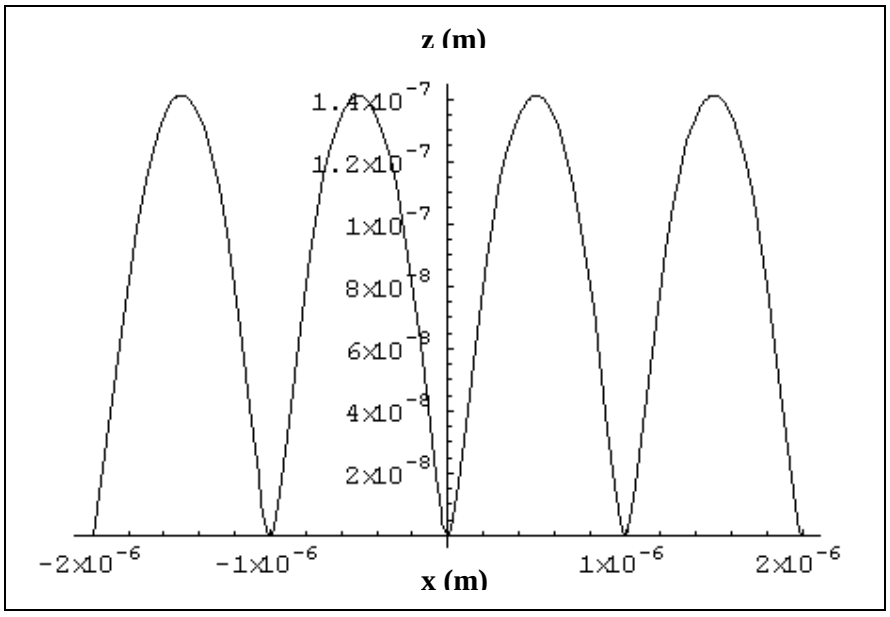

Figure 4.1 – Pattern of surface roughness for the targets morphologically modified by the electric breakdowns.

Fixing the voltage on the anode to 25 kV, the potential attains the values of 7.5 kV at a distance of 1 mm from the cathode, rapidly decreasing in a region of the thickness of the order of the surface undulations amplitude.

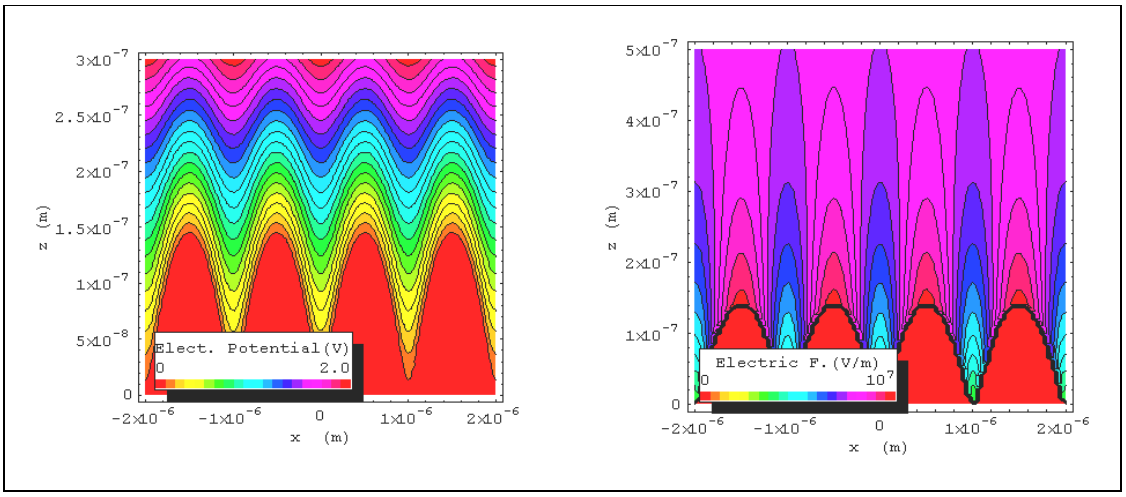

Figure 4.2 – Representation of the potential and the electric field on the cathode rough surface by MATHEMATICA.

The electric field is represented in fig. 4.3 as a function of the position on the cathode surface, varying of an order of magnitude from the valleys to the top of the whiskers. It is of the order of 1 MV/m into the valleys, while onto the tips it reaches the value of about 12.5 MV/m. For a mirror-like surface the average electric field, calculated at 25 kV of applied voltage, is about 5 MV/m.

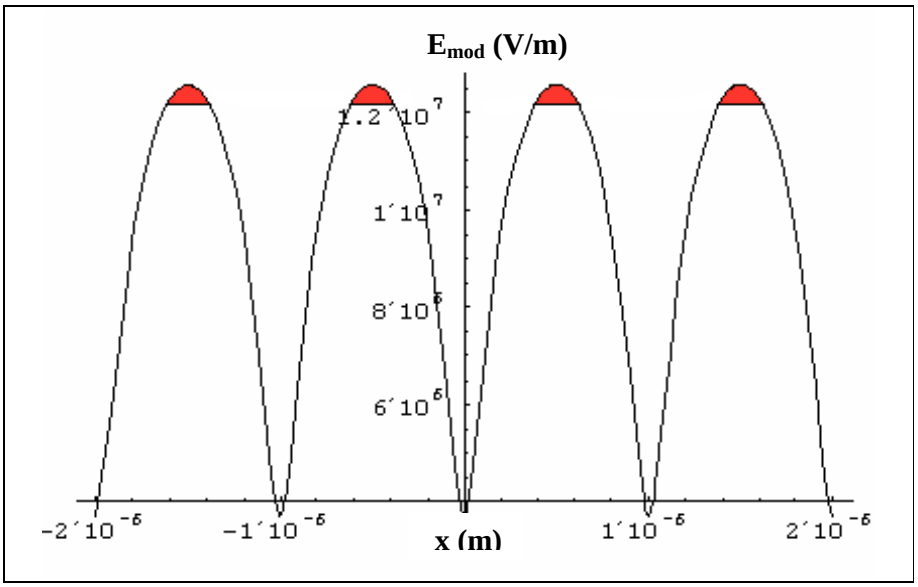

Figure 4.3 – Plot of the electric filed strength vs. the position on the cathode irregular surface.

The knowledge of the surface rate of higher electron emission, which certainly give the major contribute to the plasma generation, it is very interesting. For example, it has been found, by using the model, the surface portion with corresponds to $E > 12$ *MV/m*. From calculations, it carries out that this value is about the 8 % of the total surface area of the target (fig. 4.3). It has been calculated, besides, that approximately the 80 % of the total surface area corresponds to an electric field value higher than the one related to a mirror-like sample, under the same experimental conditions (5 MV/m).

Furthermore, it is remarkable to estimate the variation of the work function of the metal sample, for such a micro-structured inducted roughness. Thinking the superficial roughness as a series of defects in the crystal lattice, the work function is a function of the ratio n between the defects average height and their periodicity (fig. 4.4). Practically, n is the reciprocal of the *roughness coefficient* R_a defined in the eq. (3.2), and is index of the whiskers size and their periodicity on the sample surface.

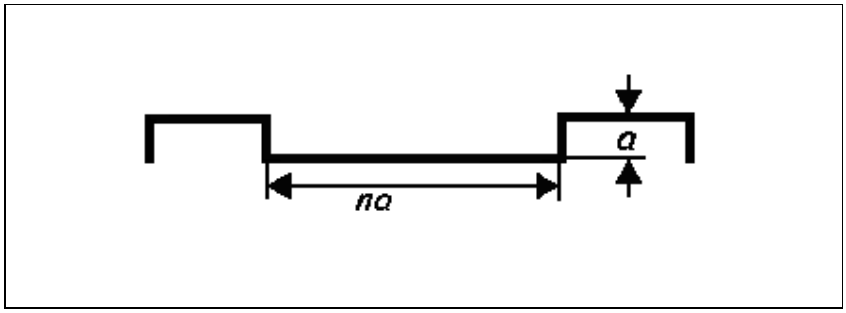

Figure 4.4 – Profile of crystal surface irregularity: n is index of defects size and their periodicity.

In fig. 4.5 it is possible to observe the percentage modification of the metal work function versus n [2]. In the following figure ϕ_0 is the work function for $n \rightarrow \infty$, namely for the ideal case of a mirror-like surface.

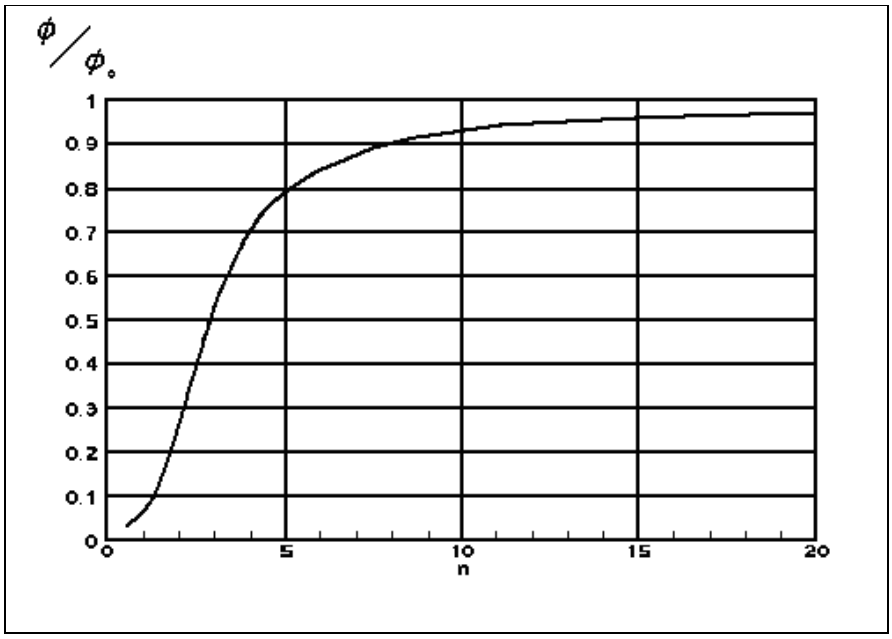

Figure 4.5 – Work function of a metal target as a function of the defect size *n*.

For the case in exam of the Y cathode with inducted micro-structured roughness, *n* is about 2 and, therefore, the work function decreases approximately of 70% with respect to a perfectly smooth surface (fig. 4.5).

4.3 Simulation by OPERA 3-D program

With the aim of visualize the electron trajectories and to get a current density map in the neighborhood of the surface tips, an electron-beam simulation was performed by means of the program OPERA 3-D. This one allowed to plan a model of rough surface with tips high 0.5 µm and large 0.3 µm, while the distance between these ones is fixed at 1 µm. This choice is compatible with the real dimensions of the whiskers, produced after the surface melting and the breakdowns stimulated by high incident laser

energies. The voltage was set to 0 on the cathode and 20 kV on the anode, while the distance anode-cathode was fixed to 5 mm. TOSCA algorithm of OPERA can be used to compute magnetostatic or electrostatic field; it determines and points out, by chromatic scales, the static fields on the contour surface of the electrodes. With the choice parameters, the resulting electric field strength is shown in the figure 4.6.

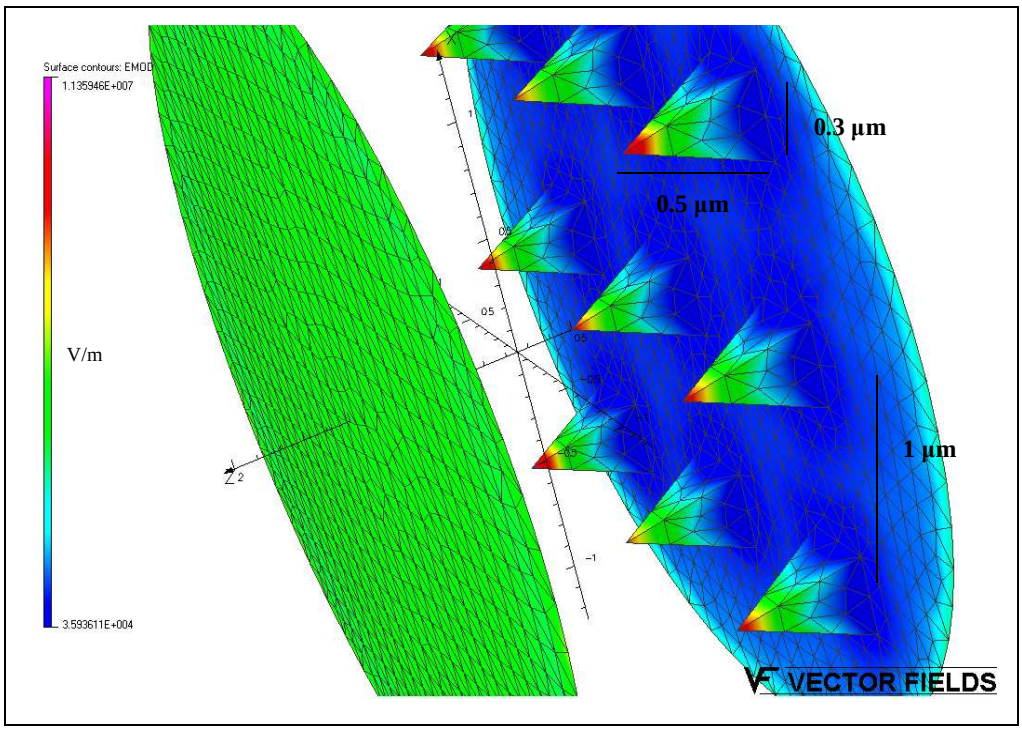

Figure 4.6 – Electric field representation on an idealized rough surface by using OPERA 3-D.

It is possible to note that the maximum electric field is reached just on the tips and values approximately 11.4 MV/m. This result is comparable with the value carried out from the above theoretical model.

In the figure 4.7 is exposed an electron-beam simulation for this geometrical model, by using SCALA algorithm of OPERA. SCALA can be used to compute the

effects caused by space charge in beams of charged particles. It provides only results for thermionic emission, therefore was set an electron emission with thermal energy $kT = h\upsilon - \phi$, where $h\upsilon$ is the laser photon energy, while ϕ is the metal work function. In this case the chosen parameters were $h\upsilon$ = 5 eV (KrF) and ϕ = 3.1 eV (Y). It is evident, from their trajectories, the high density of extracted electrons near the tips of the rough surface.

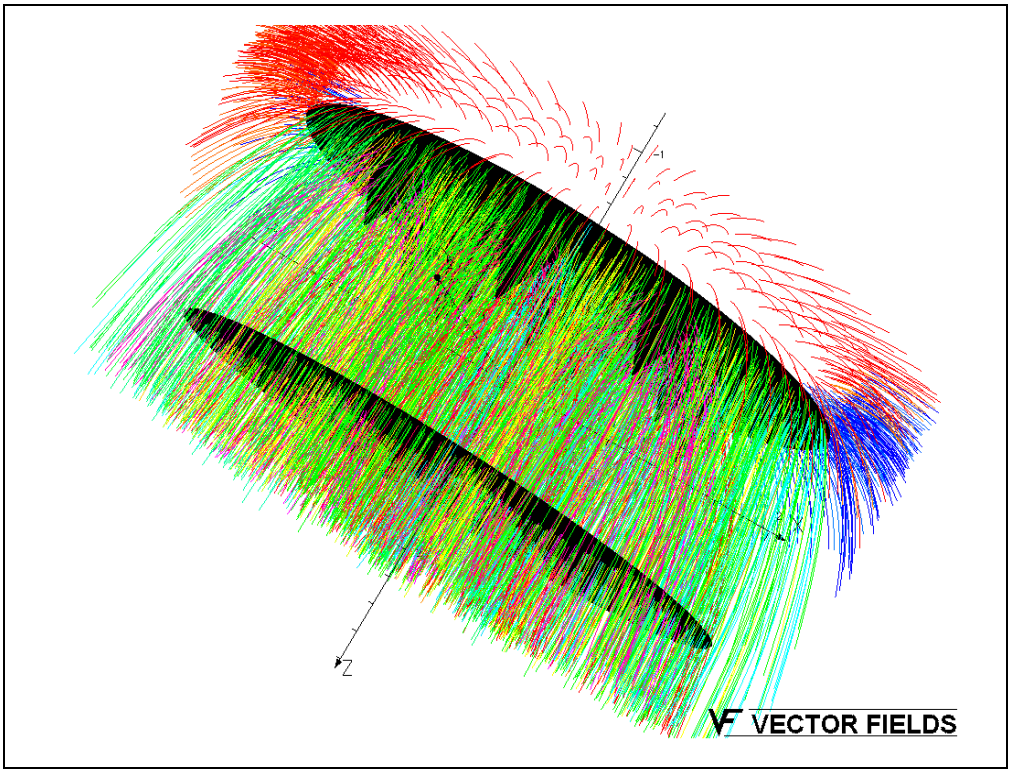

Figure 4.7 – Electron trajectories calculated by SCALA. The electrons are extracted from a sample with ideal rough surface.

SCALA supplies also the density map of the extracted current on planes parallel to the target surface. In order to avoid calculation problems due to the complexity of the geometry, it is necessary to re-plan the geometrical model with 4 pyramidal tips high

0.5 µm and large 0.3 µm; the distance between these ones is again fixed at 1 µm. Figure 4.8 shows the electron current density on a circle of 5 µm of diameter, drawn just on the top of the surface pyramids. From this pattern it is clear that the maximum for the photo-extracted current density J is about 17.9 A/cm^2, reached in the neighborhood of the tips. For the geometrical model with a mirror-like cathode, using the same experimental parameters, the simulation supplies the current density J = 2.5 A/cm^2 onto the sample surface. It is evident that the presence of the surface tips (roughness) enhances the photo-emitted current of about an order with respect to the smooth surface case.

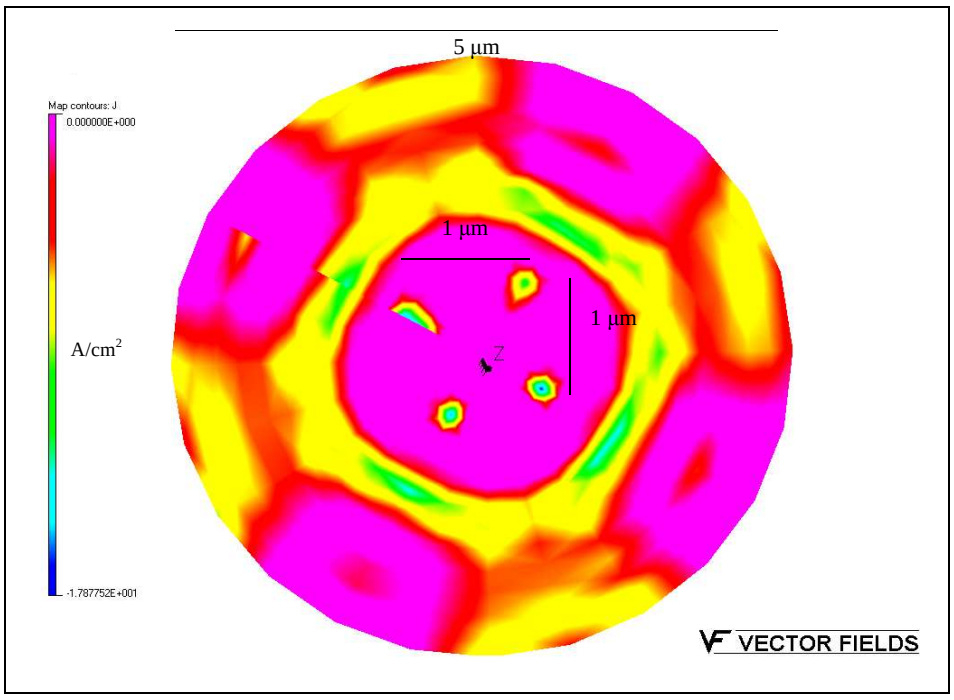

Figure 4.8 – Electron current density calculated by SCALA on a circle near the surface tips.

References Chapter 4

[1] Corless et al. *"On the Lambert W function"*, Adv. Computational Maths. **5**, 329 (1996).

[2] V.V Choulkov, *"Effect of natural roughness on electron emission from metal in electric field"*, IEEE CP **1**, 17 (2004).

5 Discussion and conclusions

5.1 Summary of experiment and simulation

In this work the electron photoemission phenomenon from metal cathodes irradiated by excimer laser source was studied in details. In particular simply experimental techniques to increase the extracted charge and, as a consequence, the emission efficiency for the target in exam, were investigated. The surface morphology, natural or induced, of the target is a fundamental parameter to determine the emission efficiency. Therefore, the cathode surface was re-modelled creating structures of the order of 1 µm, by means of high incident laser energy and electric breakdowns induced on the target. The time performance of the quantum efficiency was analyzed, because it can give important information on the microscopic process of emission. The energy sources used were three excimer lasers: XeCl, KrF and KrCl. The incidence angle laser beam-target was fixed to 0° for all the measurements. The first laser has 308 nm wavelength, 4.02 eV photon energy and 52 mm^2 spot area. The second one 248 nm wavelength, 5 eV photon energy and 43 mm^2 spot area. The third one 222 nm wavelength, 5.6 eV photon energy and 72 mm^2 spot area. The materials used like

cathodes were two metals: Zn and Y. Although the emission efficiency is higher with semiconductors, the metal targets present several advantages: low realization costs, short response time, low vacuum level to operate, angular spread of the electron beam easy handy. These benefits allows to have not-expensive electron sources of fine quality: high intensity, short pulse duration, and low emittance. These characteristic are very important for the realization of new and versatile accelerators for the industrial and medical applications: free-electron lasers, high power microwave generators, controlled thermonuclear fusion reactors, electron beam therapy machines, X-ray machines, etc.

With Zn cathode illuminated by XeCl laser at 48 mJ the obtained results were: maximum extracting current 2.3 A, maximum emission efficiency 4.5×10^{-6}. With the same target and KrF laser source at 16 mJ the data were: 11.8 A of maximum current, 1.3×10^{-4} of maximum efficiency. The best values found with KrF laser is mainly due to its higher photon energy (5 eV) with respect to the XeCl one (4.02 eV), that allows to overcome the theoretical Zn work function (4.33 eV). In both cases the plasma production on the sample surface, due to its microscopic imperfections, is emphasized at higher incident energies.

The Y cathodes used were two: the first one with smooth surface, the second one with rough surface. Before being placed in the vacuum chamber and being irradiated, the smooth target was treated by lapping-grinder machine, the rough cathode with sand-blasting machine.

The best results were obtained by using yttrium cathodes, due to their lower work function with respect to the zinc ones. The maximum extracted charge and emission

efficiency was achieved by irradiating the Y rough target with KrCl and KrF laser, respectively, after the enhancing of the surface roughness. Whisker structures of the order of 1μm were created melting the sample surface and inducing electric discharges in the anode-cathode gap. This result was obtained operatively by illuminating the target with high energy laser beams and applying high voltage between the electrodes. The entire procedure was performed without extracting the sample from the vacuum chamber. The real size of the imperfections was estimated by analyzing the SEM images and the profilometer pattern of the cathode surface after its re-modelling. After the stimulated discharges, the Y rough sample was irradiated by the same laser at 12 mJ (KrF or KrCl); the upper limit on incident energy is due to the persistence of electric breakdowns phenomena in the anode-cathode gap.

The maximum extracted current found in the entire experiment was near to 19 A, for Y rough cathode illuminated by KrCl laser at 12 mJ, after the re-modelling of its surface profile. The maximum emission efficiency, instead, was about 6.5×10^{-4}, reached under the same conditions of incident energy and target state, nevertheless by utilizing KrF laser source. The explanation of this behaviour has to be attributed to the plasma formation, which increases the photo-extracted charge. Plasma carried out from the melting of the micro-whiskers, pre-created on the cathode surface. Although the incident laser fluence was lower than the ablation threshold, the melting temperature was almost certainly reached locally on the top of the little spikes. In these points the higher electric field enhanced, for Schottky effect, the extracted current. This one, crossing the surface whiskers, provokes the plasma generation for Joule

effect. Therefore the output current entity plays a fundamental role in the plasma formation process.

Emittance calculations, executed for all the targets and the incident laser sources, have shown that the minimum angular spread for the extracted electron beam is obtained with Zn cathode irradiated by KrF laser. This behaviour, in this case, is due both to the little discrepancy photon energy-work function and to the small spot area.

The results experimentally obtained were compared with the ones carried out from a theoretical model, running with program MATHEMATICA, and a electron-beam simulation, performed by OPERA 3-D software. This operation was made with the aims to comprehend if, by modifying in another way the surface characteristics of the target, it is possible to improve the extracted electron-beam quality.

A theoretical model for the roughness profile of the sample surface was developed and the local electric field calculated. The whiskers dimension was chosen close to the real values, observed by SEM and profilometer microanalyses.

A geometrical model of surface roughness was simply created by utilizing square-base pyramids with appropriate sizes (height 0.5 μm, width 0.3 μm, distance between these ones 1 μm). Several simulations were performed by OPERA 3-D, in order to obtain electron-beam trajectories and a photo-current estimation in the neighborhood of the tips.

The electric field values found by MATHEMATICA were of 1 MV/m order in the valleys and about 12 MV/m on the top of surface whiskers, at the maximum applied voltage of 25 kV. For comparison, the average electric field for a mirror-like surface, calculated by experimental data, was 5 MV/m.

The maximum photo-current density value obtained by OPERA 3-D was approximately 18 A/cm^2, achieved for Y target irradiated by KrF laser, setting the anode voltage to 20 kV and putting the cathode to the ground. For a geometrical model with a mirror-like cathode, under the same experimental conditions, the simulation supplied J = 2.5 A/cm^2 onto the sample surface. It is evident that the presence of the surface tips (roughness) enhances the photo-emitted current of about an order with respect to the smooth surface case.

5.2 Conclusions and future developments

In this thesis work it has been demonstrated that the quantum efficiency of a metal photocathode can be higher than the value present in literature if the plasma influence is not negligible. This result depends weakly on the difference laser photon energy-target work function and the used laser intensity, but mainly on the extracted current. The surface morphology, natural or experimentally shaped, plays a fundamental role in the electron extraction process, because allows to control the plasma production and, consequently, the emission efficiency. It was found, in fact, that natural or induced micro-imperfections and superficial wishers enhance the plasma and the current density.

The surface irregularity of the target modifies the emittance values of the extracted electron beam, because of the decrease of the metal work function due to the Schottky

effect and the plasma formation on the whiskers. The combination of these two effects involve an increasing of the angular spread for the produced electron beams.

Therefore the research must be led in the direction of new systems of electron photoemission with higher intensity beams, but keeping a tolerable angular spread for the extracted electron beams.

Future work will be, therefore, the realization of metal cathodes with surface pre-treated, in order to get higher roughness with whisker-structures smaller than the 100 nm order. Of course, at the same time it is necessary to control that the angular divergence of the electron beam does not become excessive. One example of treatment is the pulsed laser deposition (PLD) of metal nano-aggregates on a bulk of the same material, by using femto-second laser. This practice might improve the extracted current intensity and, since, the quality of the generated electron-beam.